

University of Windsor

Scholarship at UWindor

Electronic Theses and Dissertations

Theses, Dissertations, and Major Papers

2012

NUMERICAL SIMULATION OF ULTRA-HIGH INJECTION DIESEL AND BIODIESEL FUEL SPRAYS

Abbas Ghasemi
University of Windsor

Follow this and additional works at: <https://scholar.uwindsor.ca/etd>

Recommended Citation

Ghasemi, Abbas, "NUMERICAL SIMULATION OF ULTRA-HIGH INJECTION DIESEL AND BIODIESEL FUEL SPRAYS" (2012). *Electronic Theses and Dissertations*. 189.

<https://scholar.uwindsor.ca/etd/189>

This online database contains the full-text of PhD dissertations and Masters' theses of University of Windsor students from 1954 forward. These documents are made available for personal study and research purposes only, in accordance with the Canadian Copyright Act and the Creative Commons license—CC BY-NC-ND (Attribution, Non-Commercial, No Derivative Works). Under this license, works must always be attributed to the copyright holder (original author), cannot be used for any commercial purposes, and may not be altered. Any other use would require the permission of the copyright holder. Students may inquire about withdrawing their dissertation and/or thesis from this database. For additional inquiries, please contact the repository administrator via email (scholarship@uwindsor.ca) or by telephone at 519-253-3000ext. 3208.

NUMERICAL SIMULATION OF ULTRA-HIGH INJECTION DIESEL AND
BIODIESEL FUEL SPRAYS

by

ABBAS GHASEMI

A Thesis

Submitted to the Faculty of Graduate Studies through
Mechanical, Automotive and Materials Engineering
in Partial Fulfillment of the Requirements for
the Degree of Master of Applied Science at the
University of Windsor

Windsor, Ontario, Canada

2012

NUMERICAL SIMULATION OF ULTRA-HIGH INJECTION DIESEL AND
BIODIESEL FUEL SPRAYS

by

ABBAS GHASEMI

APPROVED BY:

V. Roussinova

Dept. of Civil and Environmental Engineering

G.W. Rankin

Dept. of Mechanical, Automotive & Materials Engineering

R. M. Barron, Co-Advisor

Dept. of Mathematics and Statistics, and
Dept. of Mechanical, Automotive & Materials Engineering

R. Balachandar, Co-Advisor

Dept. of Civil and Environmental Engineering, and
Dept. of Mechanical, Automotive & Materials Engineering

B. Zhou, Chair of Defense

Dept. of Mechanical, Automotive & Materials Engineering

DECLARATION OF CO_AUTHORSHIP/PREVIOUS PUBLICATION

I. Co-Authorship Declaration

I hereby declare that this thesis incorporates the outcome of a joint research undertaken in collaboration with K. Fukuda under the co-supervision of Dr. Barron and Dr. Balachandar. The collaboration is covered in Chapter 2 of the thesis. In all cases, the key ideas, primary contributions, numerical simulation designs, data analysis and interpretation were performed by the author, and the contribution of co-authors in the associated publications for annual meetings, congress and conference were primarily through the provision of the numerical analysis.

I am aware of the University of Windsor Senate Policy on Authorship and I certify that I have properly acknowledged the contribution of other researchers to my thesis and have obtained written permission from each of the co-authors to include the above materials in my thesis.

I certify that, with the above qualifications, this thesis, and the research to which it refers, is the product of my own work.

II. Declaration of Previous Publication

This thesis includes three original papers that have been previously published/ submitted for publication in peer-reviewed journals and conference proceedings as indicated below:

Thesis Chapter	Publication title/full citation	Publication status
Chapter 2	Ghasemi A., Fukuda K., Balachandar R., and Barron R. Numerical Investigation of Spray Characteristics of Diesel Alternative Fuels. SAE Technical Paper 2012-01-1265, 2012* Fukuda K., Ghasemi A., Barron R., and Balachandar R., An Open Cycle Simulation of DI Diesel Engine Flow Field Effect on Spray Processes. SAE Technical Paper 2012-01-0696, 2012	Published
Chapter 3	Ghasemi A., Barron R. and Balachandar R. Spray-to-Spray Collision Break-up of Ultra-High Injection Pressure Diesel Fuel, 20th Annual Conference of the CFD Society of Canada, May 9-11, 2012, Alberta, Canada.	Presented
Chapter 2	Ghasemi A., Fukuda K., Balachandar R. and Barron R. Effect of Ultra-High Injection and Ambient Density on Diesel & Biodiesel Sprays. Green Auto Power Train AGM, November 18, 2011, Hamilton, ON, Canada.	Poster Presented
-	Fukuda K., Ghasemi A., Barron R. and Balachandar R. Numerical Simulation of Ultra-High Injection Pressure Sprays Applied to a Vertical Ports Engine Model, Green Auto Power Train AGM, November 18, 2011, Hamilton, ON, Canada.	Poster Presented

* Reprinted with permission from SAE Paper No. 2012-01-1265 © 2012 SAE International. Further use or distribution is not permitted without permission from SAE.

I certify that I have obtained a written permission from the copyright owners to include the above published materials in my thesis. I certify that the above material describes work completed during my registration as a graduate student at the University of Windsor.

I declare that to the best of my knowledge, my thesis does not infringe upon anyone's copyright nor violate any proprietary rights and that any ideas, techniques, quotations, or any other material from the work of other people included in my thesis, published or otherwise, are fully acknowledged in accordance with the standard referencing practices. Furthermore, to the extent that I have included copyrighted material that surpasses the bounds of fair dealing within the meaning of the Canada Copyright Act, I certify that I have obtained a written permission from the copyright owners to include such material(s) in my thesis.

I declare that this is a true copy of my thesis, including any final revisions, as approved by my thesis committee and the Graduate Studies office, and that this thesis has not been submitted for a higher degree to any other University or Institution.

ABSTRACT

Computational fluid dynamics (CFD) is utilized in this study to investigate the spray characteristics of diesel and biodiesel fuels. To this end, an Eulerian-Lagrangian multiphase formulation has been used to simulate the spray processes. Fuel is injected into an initially quiescent constant volume chamber. The effect of fuel type, injection pressure and ambient pressure on the spray behaviour has been studied. Macroscopic spray parameters, such as penetration and cone angle, have been investigated, and microscopic features like Sauter mean diameter, local and temporal droplet size distribution have been evaluated to further understand the spray characteristics. Results are compared with experimental data available in the literature. In addition, the interaction characteristics of two merging sprays are studied. The effects of injection point distance and incidence angle on the merged spray penetration, cone angle and Sauter mean diameter have been investigated. Different injection setups have been evaluated and compared in terms of their entrainment qualities. Finally, air motion induced by the liquid dispersion inside the spray is analyzed and connected to the entrainment.

Dedicated to

To my mother's heart, and

To my father's hands.

ACKNOWLEDGEMENTS

This thesis would not have been achievable without the valuable guidance and support of my supervisors. I would like to express my earnest and sincere gratitude to my supervisors, Dr. R. M. Barron and Dr. R. Balachandar, not only for their endless support and generous advices during this research, but also for providing me with steadfast encouragement for learning. I would also like to thank my family for being unceasingly compassionate, in every single moment of my work, from a most distant way.

I would like to express my sincere thanks to my thesis committee members, Dr G. W. Rankin and Dr. V. Roussinova for helping me with their knowledge and assistance throughout this project. I would also like to thank the Ontario Ministry of Research and Innovation for supporting this research through the Ontario Research Fund for Research excellence under the Green Auto Power Train (GAPT) project.

Finally, I would like to thank my dear friends and colleagues in the CFD lab, Kohei Fukuda, Mehrdad Shademan, Gassan Nasif, Yuanming Yu, Mo Karimi and Shabnam Jafari for supporting me throughout my research.

TABLE OF CONTENTS

DECLARATION OF CO-AUTHORSHIP/PREVIOUS PUBLICATION	III
ABSTRACT	VI
DEDICATION	VII
ACKNOWLEDGEMENTS	VIII
LIST OF TABLES	XIII
LIST OF FIGURES	XIV
ABBREVIATIONS	XVII
NOMENCLATURE	XVII
CHAPTER 1	
Introduction	1
1.1 Introduction	1
1.2 Solid Cone Fuel Spray Structure	2
1.3 Spray Modeling Approaches	8
1.4 Thesis Outline	9
CHAPTER 2	
Numerical Investigation of Spray Characteristics of Diesel Alternative Fuels	13
2.1 Introduction	13
2.2 Numerical Methodology	15

2.2.1 CFD Tool and Grid	15
2.2.2 Computational Fluid Dynamics	17
2.2.3 Spray Sub-models	17
2.2.3.1 WAVE model	18
2.2.3.2 KH-RT model	19
2.2.4 Injection and Nozzle Properties	20
2.3 Results and Discussion	22
2.3.1 Macroscopic Parametric Study of Spray	22
2.3.2 Sauter Mean Diameter (SMD)	30
2.3.3 Droplet Temporal and Spatial Size Distribution	32
2.4 Conclusions	37
CHAPTER 3	
Spray-to-Spray Collision Breakup of Ultra-High Injection Pressure Diesel Fuel	39
3.1 Introduction	39
3.2 Numerical Methodology	40
3.2.1 Computational Modeling	40

3.2.2 Grid Generation and CFD Tool	41
3.2.3 Spray Sub-models	42
3.2.4 O'Rourke Collision Model	43
3.2.5 Injection and Nozzle Properties	44
3.3 Results	46
3.3.1 Single Spray	46
3.3.2 Merging Sprays	47
3.4 Conclusions	53
CHAPTER 4	
Air Motion and Entrainment Analysis Induced by the Liquid Dispersion	55
4.1 Introduction	55
4.2 Results and Discussion	57
4.2.1 Empirical Assessment of the Entrainment in Single Sprays	57
4.2.2 Air Motion Structure Induced by Spray Dispersion	64
4.3 Conclusions	71

CHAPTER 5	
Conclusions and Recommendations	72
5.1 Conclusions	72
5.2 Contributions	75
5.3 Recommendations	75
REFERENCES	77
APPENDICES	84
Appendix I Eulerian-Lagrangian Multiphase Flow Equations	84
Appendix II Swirling Strength	85
COPYRIGHT PERMISSION	88
VITA AUCTORIS	89

LIST OF TABLES

Table 1.1 Droplet break-up regime transition Weber number (Wierzba, 1993)	8
Table 2.1 Fuel Properties (Wang et al., 2010)	21
Table 3.1 Fuel properties (Wang et al., 2010)	44

LIST OF FIGURES

Figure 1.1: Relevant processes of a fuel spray (Baumgarten, 2006)	5
Figure 1.2: Ohnesorge diagram: jet break-up regimes (Ohnesorge, 1931)	6
Figure 2.1: Grid independence check for spray tip penetration	16
Figure 2.2: (a) Nozzle geometry; (b) Injection mass flow rate profile vs. injection time (Wang et al., 2010; Huang, 2011)	22
Figure 2.3: Effect of ambient density, mesh structure and break-up model on spray tip penetration: a) 100 MPa; b) 200 MPa; c) 300 MPa	25
Figure 2.4: Influence of fuel type on spray tip penetration: a) 100 MPa; b) 200 MPa; c) 300 MPa	27
Figure 2.5: Variation of spray cone angle with injection pressure	28
Figure 2.6: Comparison of simulated and experimental (Wang et al., 2010) images of the spray at 0.45ms ASOI	29
Figure 2.7: Effect of injection pressure and ambient density on SMD in diesel fuel spray	31
Figure 2.8: Effect of fuel type on SMD	32
Figure 2.9: Droplet diameter normalized by nozzle diameter vs. droplet penetration	33
Figure 2.10: Radial distribution of particle size on different planes normal to the spray axis	35
Figure 2.11: Probability density function of droplet size distribution in different times	36
Figure 3.1: Grid independence tests	42

Figure 3.2: (a) Nozzle geometry, and (b) injection mass flow rate profile vs. injection time (Wang et al., 2010)	45
Figure 3.3: Comparison of simulated and experimental (Wang et al., 2010) images of the spray	46
Figure 3.4: Spray tip penetration; simulation (Sim) vs. experiments (Exp), (Wang et al., 2010)	47
Figure 3.5: Droplet velocity magnitude of the merging sprays at $t = 1$ ms	50
Figure 3.6: Comparison of spray tip penetration; simulation vs. experiments (Wang et al., 2010)	52
Figure 3.7: Sauter mean diameter (SMD)	53
Figure 4.1: a) Mean gas velocity field. b) Schematic evolution of the normal component of gas velocity (U_{\perp}). (Sepret et al, 2010)	56
Figure 4.2: Empirical axial variation of equivalence ratio (Wang et al. 2010)	58
Figure 4.3: Empirical Radial distribution of equivalence ratio (Wang et al., 2010)	59
Figure 4.4: Axial variation of equivalence ratio	60
Figure 4.5: Effect of injection pressure on radial distribution of equivalence ratio at an axial location of $Z = 20$ mm	61
Figure 4.6: Variation of equivalence ratio radial distribution with axial location at different injection pressures: a) 100 MPa, b) 200 MPa, c) 300 MPa	62
Figure 4.7: Effect of ambient density on equivalence ratio radial distribution at an axial location of $Z = 40$ mm	63
Figure 4.8: Single spray droplet cloud superimposed with swirling strength iso-volumes of the gas at $Z = 40$ mm	65

Figure 4.9: Turbulence intensity contour induced in the gas field in X=0 plane at Z = 40 mm for different injection pressures.	67
Figure 4.10: Velocity vector field of the air jet induced inside the spray.	68
Figure 4.11: Merging spray droplet cloud superimposed on the iso-volume of swirling strength $\left(\frac{\lambda}{\lambda_{\max}} = 0.1\right)$ at t = 1ms	70

ABBREVIATIONS

IC	Internal combustion
UHC	Unburned hydrocarbons
CFD	Computational fluid dynamics
SAE	Society of Automotive Engineers
BDFp	Palm oil biodiesel fuel
BDFc	Cooked oil biodiesel fuel
KHRT	Kelvin-Helmholtz/Rayleigh-Taylor
TAB	Taylor analogy break-up
ETAB	Enhanced Taylor analogy break-up
FIPA	Fractionnement Induit Par Accelération
SMD	Sauter Mean Diameter
ASOI	After start of injection
PDF	Probability density function
RANS	Reynolds Averaged Navier-Stokes

NOMENCLATURE

We	Weber number
ρ_l	Liquid density
d	Diameter
U_{rel}	Relative velocity
σ	Surface tension
Re	Reynolds number
μ	Viscosity

Oh	Ohnesorge number
r	Droplet radius
r_c	Child droplet radius
τ_{KH}	Break-up time
B_1	Break-up experimental constant
Λ_{KH}	Wavelength
Ω_{KH}	Kelvin-Helmholtz growth rate
U_r	Relative velocity
We_g	Gas Weber number
We_f	Liquid phase Weber number
T	Taylor number
B_0	Experimental WAVE model parameter
\mathbf{g}_t	Droplet acceleration
ρ_g	Gas density
K_{RT}	Wave number
C_τ	Model constant
d_0	Nozzle diameter
C_b	Rayleigh-Taylor model experimental constant
ρ_a	Ambient density
ΔP	Difference between injection and ambient pressures
Z	Axial locations on the spray axis
t	Time
E_{Rot}	Rotational energy of the coalesced drops

ΔE_{Surf}	Surface energy
L	Angular momentum about the centre of mass of the coalesced droplet
J	Moment of inertia
r_{eff}	Effective radius
m_1, m_2	Droplet masses
X	Off-centre distance
We_{coll}	Collision Weber number
Φ	Incidence angles
θ_{XZ}, θ_{YZ}	Spray cone angles in XZ and YZ planes
(U_{\perp})	Normal component of gas velocity
$\bar{\phi}(z)$	Average value of the equivalence ratio
$(A/F)_{st}$	Stoichiometric air/fuel ratio
C_a	Orifice area contraction
z^+	Characteristic length scale for the fuel jet
α	Shape factor for Gaussian profile
λ	Velocity swirling strength

CHAPTER 1

Introduction

1.1 Overview

Sprays are widely studied due to their vast range of scientific and industrial applications. Characteristics of fuel sprays injected into the combustion chamber of an internal combustion (IC) engine are of importance, since they influence the consequent processes of mixture formation, ignition, combustion and pollutant formation. Well-atomized fuel evaporates faster due to a longer contact time with the ambient air as well as increased interaction surface. This enhances the fuel-air mixing and increasing oxygen availability. Accordingly, the properly prepared mixture can spontaneously ignite. The combustion process of an efficient mixture leads to a maximum burning of the injected fuel. The series of events mentioned above can be very important in reducing the unburned hydrocarbons (UHC).

All the above-mentioned processes take place in a very short time. The role of an efficient break-up of the fuel jet and the droplets turns out to be even more critical in this fleeting time interval. Sprays under high injection pressures up to 200 MPa have been extensively studied both experimentally and numerically, while the need for more effective atomization suggests the application of ultra-high injection sprays. This is even more necessary for bio-diesel fuels. Bio-diesel fuels are more reluctant to break-up compared to conventional diesel fuels. The reason is due to their higher surface tension and viscosity. The surface tension force of the liquid fuel resists the aerodynamic drag forces, which are responsible for liquid jet disintegration. On the other hand, the role of viscosity is to suppress the instabilities formed on the liquid surface from growing and disintegrating the

liquid. The complexity of the multiphase phenomena occurring in the spray flows necessitates a profound understanding of the relevant processes.

There are numerous experimental studies on different features of fuel sprays. But due to the complexity of the flow field, it is not easy to thoroughly analyze all the details of the sprays with one set of experiments. Furthermore, different experimental techniques are needed to acquire information about different parameters. On the other hand, a well-established and validated numerical model provides the opportunity to investigate a variety of spray characteristics. A parametric study can be performed in a simulated environment with minimal cost and time.

1.2 Solid Cone Fuel Spray Structure

Full solid cone sprays are formed at high pressures in direct injection diesel engines. The pertinent processes are illustrated in Fig. 1.1 (Baumgarten, 2006). Occurrence of the break-up process is influenced by the flow characteristics inside the nozzle. The role of the nozzle geometry on the turbulence level at the nozzle exit, and the possible occurrence of cavitation, is significant. Higher level of turbulence at the exit can promote the instabilities at the near exit region of the fuel jet. Ultimately, the growth of these instabilities at the interface of the liquid and gas phases leads to the disintegration of the liquid jet into liquid ligaments.

There is also a possibility that the local static pressure drops below the vapor pressure of the fuel. This pressure drop usually occurs in nozzles with sharp corners. At the sharp corners of the nozzle, liquid flow is locally accelerated as a result of flow separation. This pressure drop can lead to the nucleation of the cavitation bubbles. The bubbles are transported towards the nozzle exit and, in accordance with the local flow conditions, the

bubbles may shrink, expand, or collapse. Imploded bubbles increase the turbulence level at the exit region. The collapse of the bubbles contributes to the disintegration of the fuel jet into liquid ligaments and large droplets. This is called the primary phase of break-up. This primary phase of the break-up is known as turbulence-induced break-up.

Although the contribution of the cavitation bubbles to the fuel jet break-up is beneficial to the atomization purpose, it is accompanied with some drawbacks. As illustrated in the bottom of Fig. 1.1, the cavitation region can extend towards the downstream. This extension of the vapor zone reduces the liquid effective area. The minimum cross-sectional area of the liquid is called the “vena contracta”. In the worst case scenario the vapor zone evolves downstream up to the nozzle exit. In this case the nozzle is said to be flipped. Obviously the negative effect of the cavitation is the reduction of the liquid effective area. Consequently, the effective injection mass flow rate decreases. This might result in lower accumulated heat release and power generation of the internal combustion engines.

After the primary phase of the break-up, farther downstream, as a result of the dominance of the aerodynamic forces (over the surface tension force), the larger droplets break up into smaller ones in the secondary break-up phase. The secondary phase is commonly called the aerodynamic-induced break-up. As a result of the velocity difference at the shear layer of the liquid jet, the gas-liquid interface becomes unstable. The amplitude and frequency of these instabilities are dependent on the gas and liquid properties and the flow conditions. Eventually, if the instabilities are not dampened by the viscous forces, they dominate the surface tension forces and disintegrate the liquid.

Due to the roll-up of the liquid shear layer, ambient air is engulfed into the spray and the mixing process starts. This is called the entrainment process. A significant part of the air

entrainment occurs at the tip of the spray. If the spray is injected into an initially quiescent chamber, the entrainment process sets the stagnant air into motion in the form of secondary vortex field. Entrainment of ambient air and the radial movement of the low kinetic energy droplets towards the outside region expand the spray in the spanwise direction. This results in a conical shape of the spray.

Larger and faster droplets are located in the dense region near the spray axis, while the droplets become smaller and slower as a result of aerodynamic interaction with the continuous phase near the outside area. Droplets located in the near-field and around the spray axis are subjected to a higher number of collisions in the dense region. Higher number of collision can result in the coalescence of the droplets. In the downstream zone where the droplets have sufficiently atomized, depending on the ambient temperature, the evaporation of the droplets can be the dominant process in the mixture formation.

It is worth to mention that the above explained series of processes are for a single component fuel. In a real diesel fuel, which is multi-component, some additional features are to be considered. One of the interesting processes in multi-component fuel is the thermodynamic break-up. Depending on the local flow conditions, the pressure might drop below the vapor pressure in one of the components. Therefore, there is a possibility of flash boiling of that component. This abrupt evaporation disintegrates the fuel and enhances the break-up.

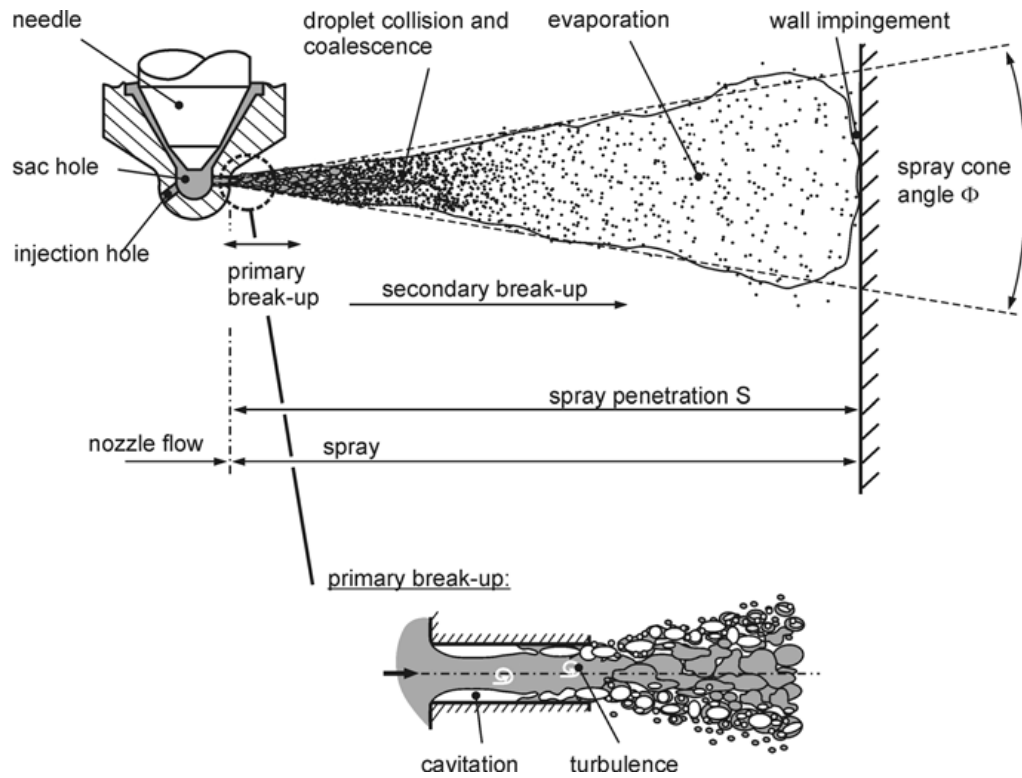


Figure 1.1: Relevant processes of a fuel spray (Baumgarten, 2006)

In order to develop an assessable explanation of the multiphase flow of a fuel jet, the Weber number is used to connect the flow parameters of the discrete (liquid) and continuous (gas) phases. Weber number is defined as $We = \frac{\rho_l d U_{rel}^2}{\sigma}$, where ρ_l , d , U_{rel} and σ are fuel density, droplet diameter, relative velocity and surface tension, respectively. Weber number defines the ratio of the inertial forces to the surface tension forces of the liquid phase. Disintegration of the jet commences when the aerodynamic forces dominate the liquid surface tension. As can be seen in Fig 1.2, Ohnesorge (Ohnesorge, 1931) categorized multiphase jet flow regimes based on the Reynolds number, defined as $Re = \frac{\rho_l d U_{rel}}{\mu}$, and the Ohnesorge number, defined as $Oh = \frac{\sqrt{We}}{Re}$.

Higher injection pressures result in larger relative velocities. Therefore, larger instabilities are formed at the liquid-gas interface. In addition, higher relative velocities result in larger aerodynamic drag forces acting on the liquid from the gas phase. In a high Reynolds number spray, viscosity is not large enough to dampen the instabilities. On the other hand, in a high Weber number condition, surface tension forces cannot resist the aerodynamic forces. Eventually, these conditions shift the fuel jet regime into the atomization zone of Fig. 1.1. High injection pressure sprays utilized in internal combustion engines fall into the atomization category due to the larger relative velocity and Weber number. Therefore, it is important that any numerical modelling be capable of resolving the typical phenomena taking place.

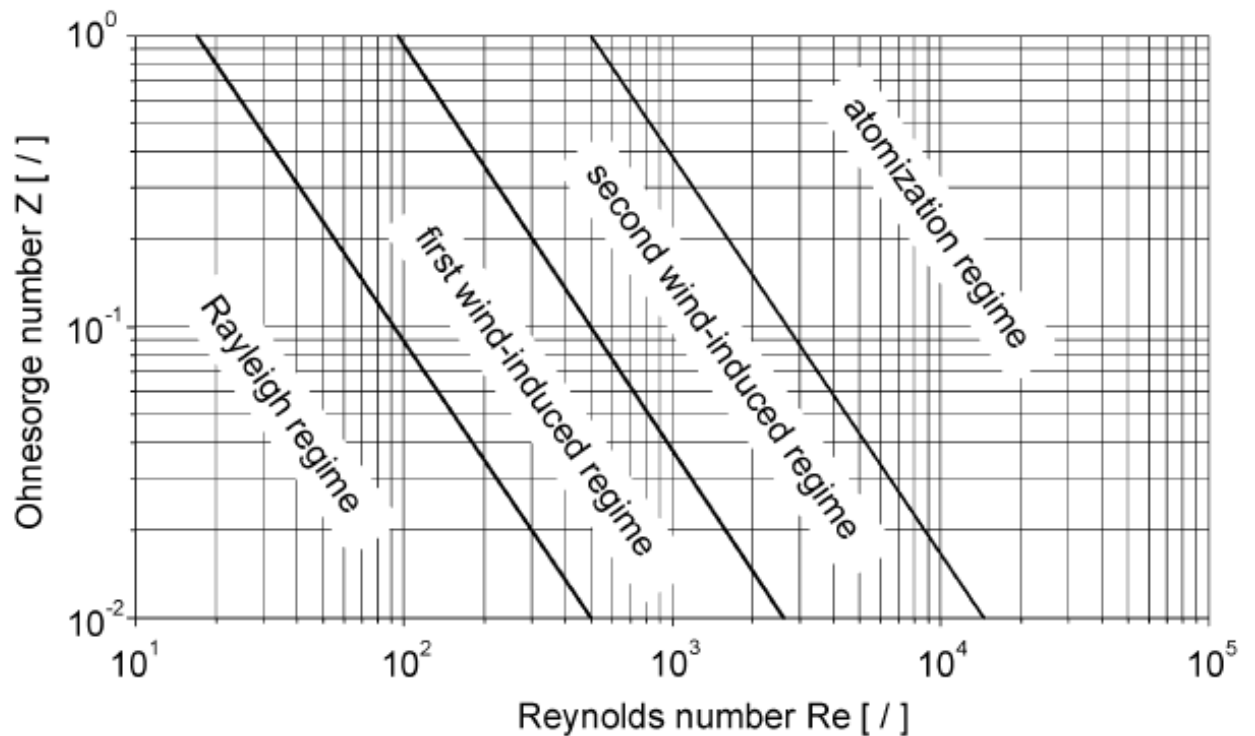























Figure 1.2: Ohnesorge diagram: jet break-up regimes (Ohnesorge, 1931)

After identifying the jet flow regime, it is essential to determine the droplet break-up regime. This classification can be done according to Wierzba (1993), as presented in Table 1.1. At different Weber numbers it is expected that instability waves at the interface of the liquid and gaseous phases develop with different amplitudes and wavelengths. Individual break-up regimes are connected to the instability waves formed in the droplet surface. At $We \approx 12$ the vibrational type of break-up occurs. Lower than this critical value, droplet deformations do not lead to break-up. In the bag break-up mode, $12 < We < 20$, deformation of the droplet into a bag form causes the break-up. The edge of the bag breaks into larger droplets while the remaining parts form small droplets. Therefore, a bimodal size distribution is observed. An extra jet emerges at $20 < We < 50$, resulting in bag-jet (bag-streamer) break-up. At $50 < We < 100$, droplet diameter decreases bit by bit due to the shedding of the child droplets from the shear layer of the parent droplet as a result of the shear forces. This regime is called stripping. The catastrophic break-up regime appears in two steps and at $We > 100$. As a result of an intense drag force, droplets break up into droplets which are fairly large due to large amplitude and wavelength of the instability surface waves. Simultaneously, smaller droplets are shed from the liquid surface because of the short wavelengths. It should be mentioned that this transition Weber numbers to different droplet break-up regimes are not consistent in the literature and also they can be categorized differently (Baumgaerten, 2006).

Table 1.1 Droplet break-up regime transition Weber number (Wierzba, 1993)

Droplet break-up regime		We	Schematic (Baumgarten, 2006)				
I.	Vibrational	≈ 12					
II.	Bag	< 20					
III.	Bag-jet (Bag-streamer)	< 50					
IV.	Stripping	< 100					
V.	Catastrophic	> 100					

1.3 Spray Modeling Approaches

After ascertaining the jet and droplet break-up regimes, an appropriate solution technique must be selected. Various spray simulation methods can be chosen depending on the flow regime, application, and the focus of the study. Different approaches are classified according to the manner of flow simulation, as Eulerian, Lagrangian or Eulerian-Lagrangian methods. There are also different kinds of interface modeling methods such as capturing or tracking. In addition, either integrated or segregated flow-interface coupling techniques can be utilized. Furthermore, the approaches can be categorized

according to the types of spatial discretization schemes, such as meshless, finite difference, finite volume or finite element (Ashgriz, 2011).

In the Eulerian-Lagrangian method the continuous (gaseous) phase is treated in an Eulerian framework while the discrete (liquid) phase is handled by the Lagrangian formulation. Navier-Stokes equations are solved, coupled with an appropriate turbulence model, to describe the flow field of the continuous phase in a fixed grid system. On the other hand, the discrete liquid phase is defined using a Lagrangian meshless particle tracking method.

Various sub-models are responsible for outcomes of turbulent dispersion (Gosman & Ioannides, 1981), coalescence (Ashgriz & Poo, 1990), evaporation (Faeth, 1983) and droplet break-up (Wierzba, 1993) in the fuel spray simulation. The discrete and continuous phases persistently exchange momentum, energy and mass. Influence of the discrete phase on the continuous phase is applied as source terms in the conservation equations of the gas phase in each grid cell. On the other hand, the continuous phase influences the discrete phase by using the local values of temperature, gas velocity, etc., of the grid cell through which the droplet is passing at each time step as a boundary condition (Baumgarten, 2006).

1.4 Thesis Outline

This thesis reports on computational fluid dynamics (CFD) simulations of ultra-high injection pressure diesel and bio-diesel sprays. The emphasis of the research is to create a numerically accurate model, capable of predicting different aspects of fuels sprays. Numerical set-up for the study was implemented in the ANSYS Fluent 13.0 CFD package.

The problem under investigation is categorized as a multiphase flow, and a concise report of the importance and applications of the problem has been provided in Chapter 1. Moreover, relevant processes observed in a full cone fuel spray and the governing mechanisms are described. An explanation about the Eulerian-Lagrangian approach has been provided since it is the technique which has been selected to deal with the multiphase nature of the problem due to its feasibility in modelling the processes occurring in a diesel spray.

In Chapter 2, the effect of injection and ambient parameters on spray break-up and atomization of different alternative fuels are investigated using CFD simulation. Due to increasingly strict emission regulations for IC engines, there is a significant motivation to use biodiesel fuels instead of the conventional diesel fuels with the objective to reduce the exhaust gas emissions. Spray characteristics play a progressively important role in the consequent processes of mixture formation, ignition, combustion and pollutant formation in direct injection diesel engines. It is also important to develop an understanding of the atomization qualities of alternative fuels such as biodiesels as potential substitutes for conventional diesel fuel.

An Eulerian-Lagrangian approach is implemented to study the interaction of the continuous and discrete phases. Numerical simulations are extensively validated via experimental data available in the literature for a constant volume chamber under ultra-high injection conditions up to 300 MPa. Simulated spray tip penetration, spray cone angle and spray images are compared with experiments and analytical correlations for three fuel types (diesel, palm oil and cooked oil), three injection pressures (100, 200 and 300 MPa), and two ambient densities (15 and 30 kg/m³). Effect of mesh structure and two

break-up models (WAVE and KHRT) on spray penetration are also investigated. Droplet size distribution in the radial and axial directions is studied. The contents of Chapter 2 have been published as a technical paper in Society of Automotive Engineers (SAE) 2012 World Congress (Ghasemi et al., 2012-a). As such, Chapter 2 has its individual introduction, literature review, numerical methodology, model description, discussion of results discussion and conclusion sections.

Another interesting topic of study is the interaction of two merging sprays, the characteristics of which has not been studied as much as single sprays. This topic has been studied in Chapter 3. Mixture formation is highly influenced by the atomization process of the fuel spray in a direct injection IC engine. In order to achieve higher levels of droplet atomization, ultra-high injection pressures are utilized. The focus of Chapter 3 is on the collision break-up process provided by two interacting fuel jets. The first step is to simulate a single spray injected into an initially quiescent constant volume chamber using the Eulerian-Lagrangian approach. Reynolds-Averaged Navier-Stokes equations, accompanied by the $k - \varepsilon$ turbulence model, are solved using an Eulerian formulation of the continuous phase. The discrete droplet phase is treated using a Lagrangian formulation together with spray sub-models. Results are validated via experimental results available in the literature. The second step is to study the effect of incidence angle and separation distance of interacting sprays on the spray parameters such as tip penetration and Sauter mean diameter (SMD). Spray tip penetration is redefined based on the temporal development of the tip of the merged spray. Injection pressures up to 300 MPa are applied to an ambient air pressure of 1.27 MPa. The contents of Chapter 3 have been presented in the 20th Annual Conference of the CFD Society of Canada (Ghasemi et

al., 2012-b). Chapter 3 has its individual introduction, literature review, computational modeling, results and discussion, and conclusion sections. In addition, further investigation is performed in Chapter 4 to achieve a deeper understanding about the entrainment characteristics of the interacting sprays compared to single sprays.

Finally, in Chapter 5 an overall summary of the discussions and conclusions resulting from the previous chapters is presented.

CHAPTER 2

Numerical Investigation of Spray Characteristics of Diesel Alternative Fuels

2.1 Introduction

Direct injection diesel engine technology has been considerably enhanced in order to be able to pass the strict emission and performance regulations and standards set by governments. Many researchers, e.g., Som & Aggarwal (2010), Dhuchakallaya & Watkins (2011), Zhang & Fang (2011), Demoulin & Borghi, (2002), have shown that spray injection parameters have a strong effect on the processes of evaporation, mixture formation, ignition, combustion and pollutant formation in diesel engines.

CFD simulation serves as a useful tool in acquiring a better understanding of the above mentioned processes. The internal nozzle flow features caused by the geometrical effects of the nozzle have been studied by Som et al. (2011), Som et al. (2010) considered the effects of cavitation, Lee & Reitz (2010) examined turbulence effects and Trinh & Chen (2007) conducted research on the spray development and break-up. Among many multiphase spray modeling methods (Ashgriz, 2011), Divis & Macek (2005) investigated these effects numerically using an Eulerian-Eulerian formulation and Wang et al. (2011) used a Lagrangian-Eulerian approach.

In order to investigate primary and secondary phases of the break-up process, various break-up models like Taylor Analogy Break-up (TAB), Enhance TAB (ETAB), WAVE, Kelvin-Helmholtz-Rayleigh-Taylor (KH-RT) and Fractionnement Induit Par Acceleration (FIPA) have been proposed and utilized by researchers to investigate characteristics of diesel sprays (Djavareshkian & Ghasemi, 2009; Fu-Shui et al., 2008). Ambient fluid characteristics like pressure (Roisman et al., 2007), temperature (Park et al., 2010), and combustion chamber flow field pattern (Ghasemi & Djavareshkian, 2010), affect spray behaviour.

By influencing the aerodynamic interaction of the continuous and discrete phases and air entrainment rate into the spray, combustion and pollutant formation can be altered. In order to achieve higher levels of atomization and mixture formation to provide a more homogeneous mixture which contributes to better combustion efficiencies and lower production of particulate matters, utilizing high and ultra-high fuel injectors are of great interest. Accordingly, spray parameters such as penetration, Sauter Mean Diameter (SMD) and spray cone angle have also been studied (Bianchi et al., 2001).

Due to price issues associated with petroleum fuels as well as emission concerns, biodiesel fuels are emerging as alternatives for traditional fuels. As a consequence, spray (Park et al., 2009), combustion (Jaime et al., 2010) emission (Lin & Lin, 2011), and characteristics of fuels like various types of biodiesel and dimethyl ether (Kim et al., 2010) have been studied to provide sufficient knowledge of their behaviour in diesel engine environments and operating conditions.

The objective of the present work is to numerically study the spray behaviour and characteristics of ultra-high injection diesel fuel and the biodiesel fuels palm oil (BDFp) and cooked oil (BDFc). Simulation results have been validated using the experiments performed by Wang et al. (2010) in a constant volume chamber. Effects of injection and ambient pressure, fuel type and mesh structure on the spray penetration are studied. For the different cases, the predicted spray cone angle is compared with experiments at a certain time after the start of the injection. Two break-up models, WAVE and KH-RT (Kelvin-Helmholtz-Rayleigh-Taylor), are used to see the effect of break-up on the spray modeling. As a criterion for spray break-up and global droplet size, Sauter Mean Diameter (SMD) variation with time is also computed and compared with the experiments. Since SMD only represents global information about droplet size, a droplet size distribution and probability density function analysis is also performed to achieve an understanding of the temporal and spatial droplet size variation.

2.2 Numerical Methodology

2.2.1 CFD Tool and Grid

Simulations have been carried out using ANSYS FLUENT 13 by modeling a constant volume chamber of size ($60\text{ mm} \times 60\text{ mm} \times 80\text{ mm}$). The first step in the mesh selection and generation was to perform simulations on different fully structured meshes with 5×10^5 to 1.8×10^6 cells in order to achieve grid independence. Based on the results for the penetration depth vs. time after start of injection (ASOI) shown in Fig. 2.1, the $1\text{ mm} \times 1\text{ mm} \times 0.2\text{ mm}$ mesh, referred to as M_1 with 1.44×10^6 cells, was selected. But, in order to overcome the issue associated with the susceptibility of particle tracking

methods to mesh structure, in terms of predicting turbulent dispersion of the particles (Merker et al., 2006), which leads to the miscalculation of the spray characteristics, a second mesh M_2 of size $0.5\text{mm} \times 0.5\text{mm} \times 0.8\text{mm}$ was generated. In this step, the ratio of the cell size in the spray axial to radial directions was changed while keeping the cell number constant (equal to M_1), to achieve optimum numerical and experimental correspondence. The comparison of M_1 and M_2 results are reported in the following sections.

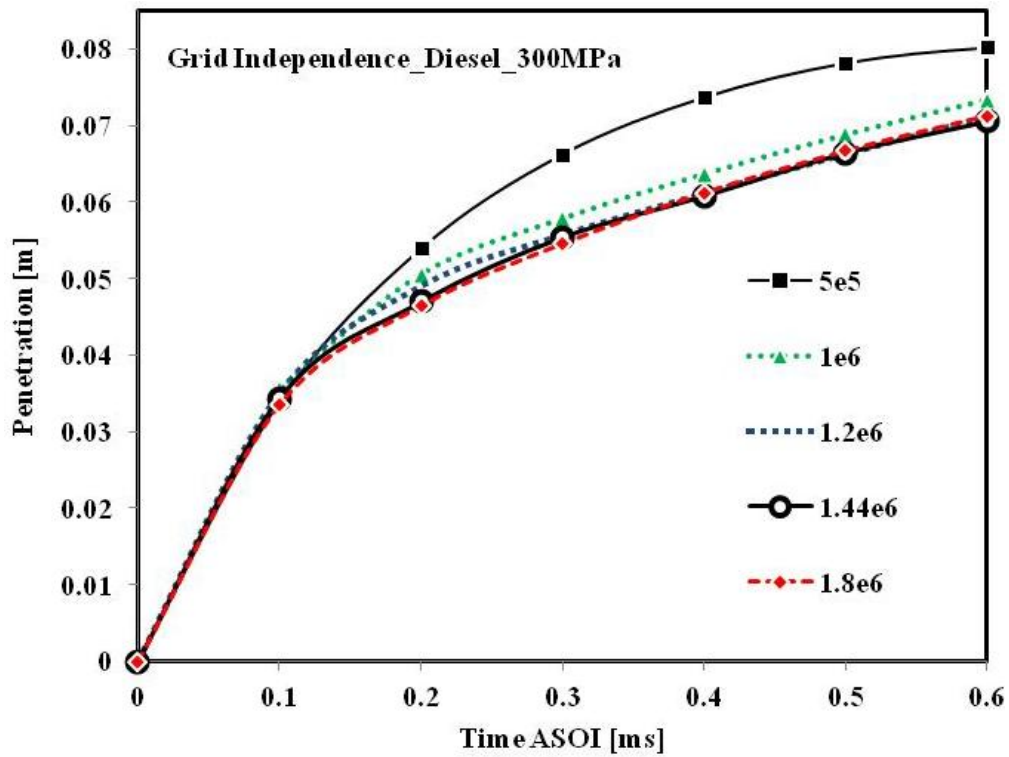


Figure 2.1: Grid independence check for spray tip penetration

2.2.2 Computational Fluid Dynamics

A Lagrangian-Eulerian multiphase formulation has been utilized in order to simulate the interaction of the discrete and continuous phases. The Navier-Stokes equations are solved for the continuous gas phase using $k - \varepsilon$ turbulence model. At each time step ($\Delta t = 1 \times 10^{-6}$ s), the Eulerian approach defines the flow parameters such as velocity components, pressure, density and temperature as a function of position (x,y,z) for the entire three-dimensional flow domain. In a Lagrangian description, the droplets are assumed as single mass particles, the velocity of which is decelerated by aerodynamic interaction of the gas and droplet, the mass of which is decreased by evaporation, etc. The two phases continuously exchange momentum, energy and mass. These exchanges are accounted for by applying source terms in the conservation equations of the gas phase in each grid cell. On the other hand, the gas phase affects the dispersed liquid by employing the local values of temperature, gas velocity, etc., in the grid cell through which the droplet is passing at each time step as a boundary condition. In Eulerian-Lagrangian method it is assumed that the volume fraction of the discrete phase is small compared to the continuous phase (Baumgarten, 2006). Details of the Eulerian-Lagrangian approach formulation is presented in appendix I.

2.2.3 Spray Sub-models

Various sub-models have been implemented to account for the effects of coalescence (Ashgriz & Poo, 1990), evaporation (Faeth, 1983) and droplet break-up (Wierzbna, 1993) in the fuel spray simulation. Two break-up models which are discussed in more details in the next subsections are also used. It should be mentioned that both of the break-up

models used assume the liquid and gas phases to be incompressible. A turbulent dispersion model (Gosman & Ioannides, 1981) accounts for the interaction of the droplets with the turbulent eddies in the gas phase. Fluctuating motion of the droplets due to these interactions are superimposed on their mean velocity. These fluctuations contribute to an enhanced mixing of the liquid and gas.

2.2.3.1 WAVE model

In the WAVE or Kelvin-Helmholtz (KH) model (Reitz & Diwakar, 1987), growth of an initial disturbance on the liquid surface due to the Kelvin-Helmholtz instability generated at the aerodynamic interaction surface of the liquid and gas is related to the wavelength of the fastest growing wave and to the other physical and dynamic parameters of the injected fuel and the ambient fluid to estimate the break-up time and child droplet size. The rate of droplet size variation is given by:

$$\frac{dr}{dt} = \frac{r-r_c}{\tau_{KH}} \quad (1)$$

where r is the droplet radius, r_c is the child droplet radius and τ_{KH} is the break-up time,

$$\tau_{KH} = \frac{3.762B_1r}{\Omega_{KH}\Lambda_{KH}} \quad (2)$$

Here B_1 is an experimental constant, Λ_{KH} is the wavelength of the fastest growing wave and Ω_{KH} is the growth rate. Both Λ_{KH} and Ω_{KH} depend on the local flow properties:

$$\Omega_{KH} = \frac{0.34+0.38We_g^{1.5}}{(1+0h)(1+0.4T^{0.6})} \sqrt{\frac{\sigma}{\rho_f r^3}} \quad (3)$$

$$\Lambda_{KH} = 9.02r \frac{(1+0.45\sqrt{Oh})(1+1.4T^{0.7})}{(1+0.865We_g^{1.67})^{0.6}} \quad (4)$$

In eqns. (3) and (4), σ is the surface tension, ρ_f is the liquid density, $We_g = \rho_f U_r^2 / \sigma$ represents the gas Weber number, where U_r is the relative velocity between the liquid and gas, $Oh = \sqrt{We_f} / Re_f$ is the Ohnesorge number, where We_f is the liquid phase Weber number and Re_f is the liquid phase Reynolds number, and $T = Oh \sqrt{We_g}$ is the Taylor number. The diameter of the child droplet is defined as:

$$r_c = B_0 \Lambda_{KH} \quad (5)$$

where B_0 is an experimental model parameter set to 0.61.

2.2.3.2 KH-RT model

In contrast to the WAVE model, the hybrid KH-RT (Kelvin-Helmholtz-Rayleigh-Taylor) model is capable of distinguishing between primary and secondary break-up processes (Beale & Reitz, 1999). The Rayleigh-Taylor (RT) model describes the droplet break-up due to the instabilities generated at the liquid gas interface due to the density difference. In this model, the frequency Ω_{KH} and wavelength Λ_{KH} of the fastest growth wave generated by the RT instability are given by

$$\Omega_{KH} = \sqrt{\frac{2}{3\sqrt{3}\sigma} \frac{|-g_t(\rho_f - \rho_g)|^{1.5}}{\rho_f + \rho_g}} \quad (6)$$

$$\Lambda_{KH} = \frac{2\pi}{K_{RT}} \quad (7)$$

Here g_t is the droplet acceleration, ρ_g is the gas density and K_{RT} is the wave number corresponding to Λ_{KH} , defined as:

$$K_{RT} = \sqrt{\frac{|g_t(\rho_f - \rho_g)|}{3\sigma}} \quad (8)$$

In the RT model, the time starts to be recorded when the diameter of the droplet is larger than the wavelength Λ_{RT} . The break-up is calculated if this time is longer than the RT model break-up time, which is calculated as follows:

$$\tau_{RT} = \frac{C_\tau}{\Omega_{RT}} \quad (9)$$

where C_τ is a model constant set to 1. The droplet radius in the RT model is calculated from

$$r_{RT} = \frac{\pi C_{RT}}{K_{RT}} \quad (10)$$

where C_{RT} is a model constant set to 1. Before the break-up length is reached, the KH model is applied. Farther downstream the KH and RT models have a competing effect on the break-up.

The break-up length is defined as:

$$L_b = C_b d_0 \sqrt{\frac{\rho_f}{\rho_g}} \quad (11)$$

where d_0 and C_b are the nozzle diameter and an experimental constant, respectively. The value of C_b is estimated as

$$C_b = 0.5B_{b1} \quad (12)$$

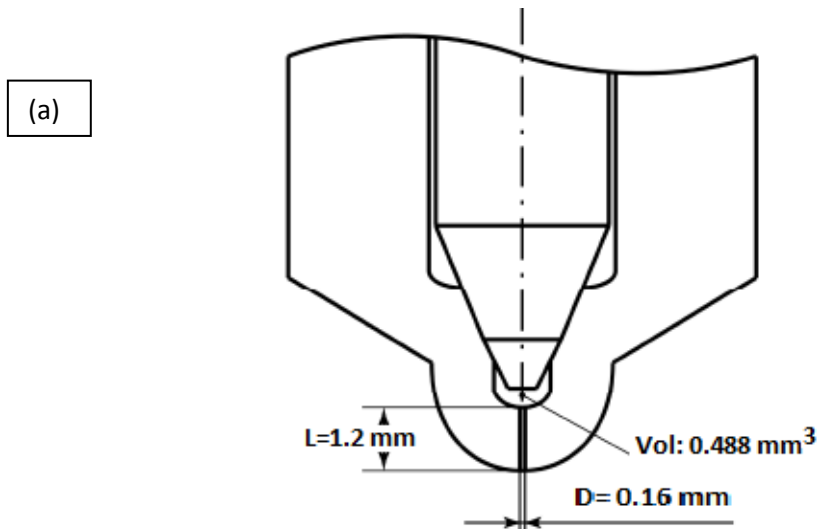
2.2.4 Injection and Nozzle Properties

A single hole 160 μm diameter nozzle with a nozzle hole length-to-diameter ratio of 7.5 was used to inject the fuels with 100, 200 and 300 MPa injection pressures into the 295K quiescent ambient air of 15 and 30 $\frac{Kg}{m^3}$ density (corresponding to 1.27 and 2.54 MPa).

Fuel properties are shown in Table 2.1. The injector geometry and the variable mass flow rate profile applied to the simulations as inlet boundary condition for the discrete phase model are shown in Fig. 2.2.

Table 2.1 Fuel Properties (Wang et al., 2010)

Fuel type	Diesel	BDFp	BDFc
Density ($\frac{Kg}{m^3}$) @ 15 °C	830	874.4	885.1
Viscosity ($\frac{mm^2}{s}$) @ 30 °C	3.36	5.53	4.45
Surface tension ($\frac{mN}{m}$)	25.5	26.2	25.7
Cetane Number	55	64.6	49.9
Heating value ($\frac{MJ}{Kg}$)	43.1	40.03	39.03



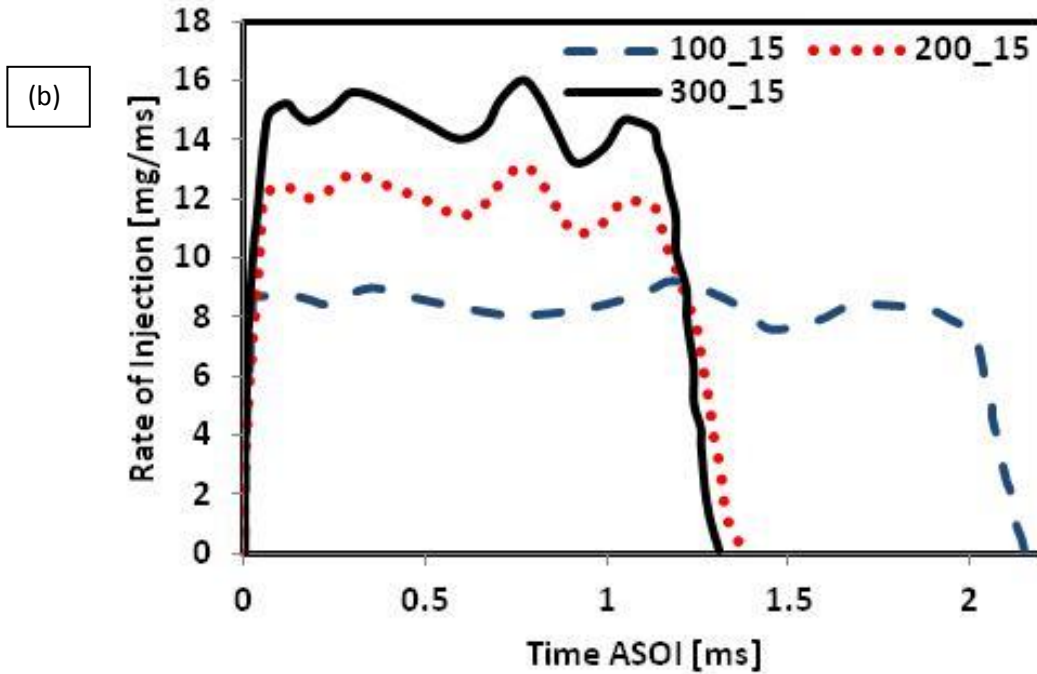


Figure 2.2: (a) Nozzle geometry; (b) Injection mass flow rate profile vs. injection time

(Wang et al., 2010; Huang, 2011)

2.3 Results and Discussion

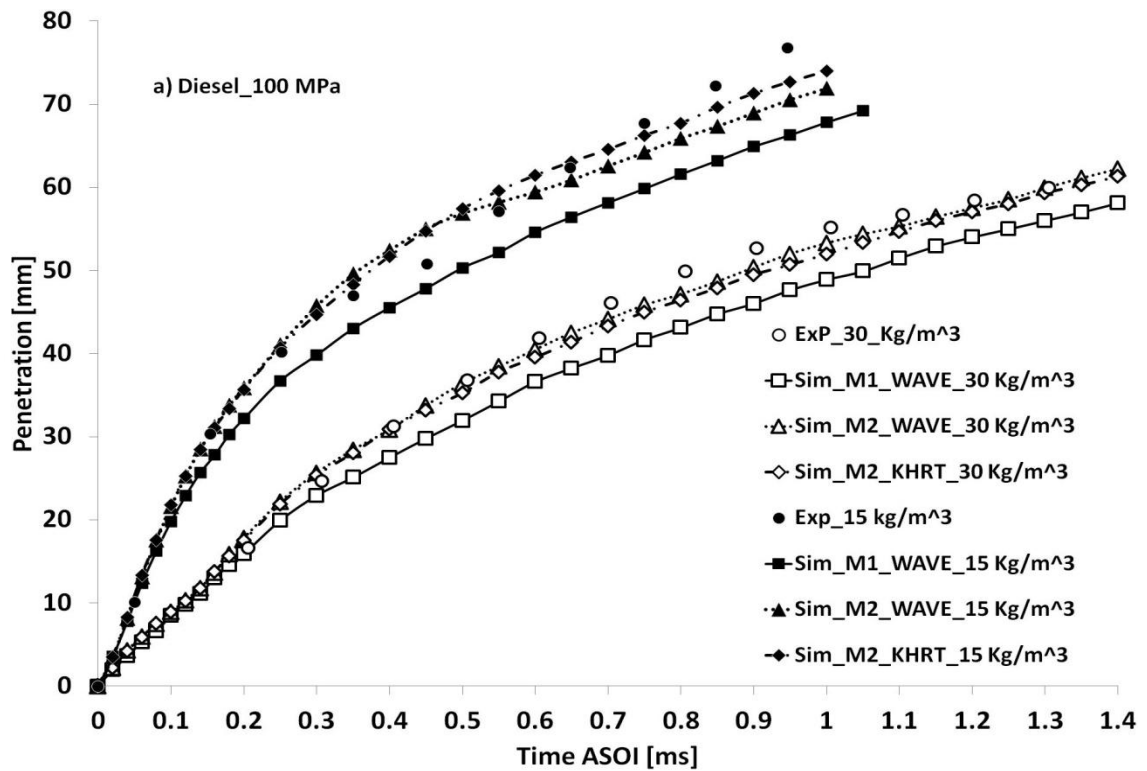
2.3.1 Macroscopic Parametric Study of Spray

Figure 2.3 shows the temporal development of the spray tip into the chamber including the effects of ambient density, mesh structure and break-up model. It should be mentioned that for each case the simulation results are presented up to the time the spray reaches the end wall of the chamber. The reason is that in this study a free spray is simulated and wall impingement is not considered. Spray tip penetration consists of a linear phase which is converted into an asymptotic behaviour due to the aerodynamic deceleration of the tip. Tip penetration is usually defined as the maximum distance of 97% of the droplets from the nozzle at each time t . Obviously the spray tip travels faster at higher injection pressures. But, for a certain injection pressure, higher ambient density

(pressure) provides larger drag force and stronger resistance to the droplet movement and inhibits the axial penetration. In Lagrangian-Eulerian particle methods there is an issue in regards to penetration that needs to be discussed. Prediction of the particle dispersion, which directly affects parameters like penetration and spray cone angle, is very sensitive to mesh structure. Although the grid independence check was performed in terms of the cell number, the M_1 mesh still under-predicts the penetration due to the over-prediction of the droplet radial dispersion of the particles. Usually this issue is resolved using mesh clustering in the axial and radial directions (Merker et al., 2006). Here, we deal with this problem in an alternative way by changing the axial-to-radial ratio of the cell size while keeping the cell number constant. As can be seen in the case of the M_2 mesh, which has a higher axial-to-radial cell size ratio compared to M_1 , a higher jet penetration (lower radial particle dispersion) occurs. In the case of break-up models it can be seen that WAVE and KH-RT provide close results, but in some cases KH-RT has a lower prediction of the penetration at the final stage of the spray tip evolution. WAVE as a classic breakup model and KH-RT as a hybrid model both treat the primary break-up based on the Kelvin-Helmholtz instability. Accordingly, spray penetration displays model independence at the early stages of injection because in this phase spray penetration is more dependent on the large, high momentum droplet velocity. But farther downstream, droplet size and break-up become more influential on the penetration, after which the competing effects of the KH and RT models govern the break-up process and consequently the penetration.

The influence of fuel type on spray tip penetration is illustrated Fig. 2.4. Referring to the fuel properties in Table 2.1, it can be seen that fuels with larger surface tension have traveled more into the ambient fluid. Higher surface tension means that at a similar gas

density, injection relative velocity, and initial droplet size (blob size equal to nozzle size in this case), a lower Weber number is achieved. Weber number is one of the key factors in the estimation of the droplet break-up time. In particular, droplets with lower Weber number which are subjected to lower aerodynamic drag relative to their surface tension would have a larger residence time and travel farther in the chamber.



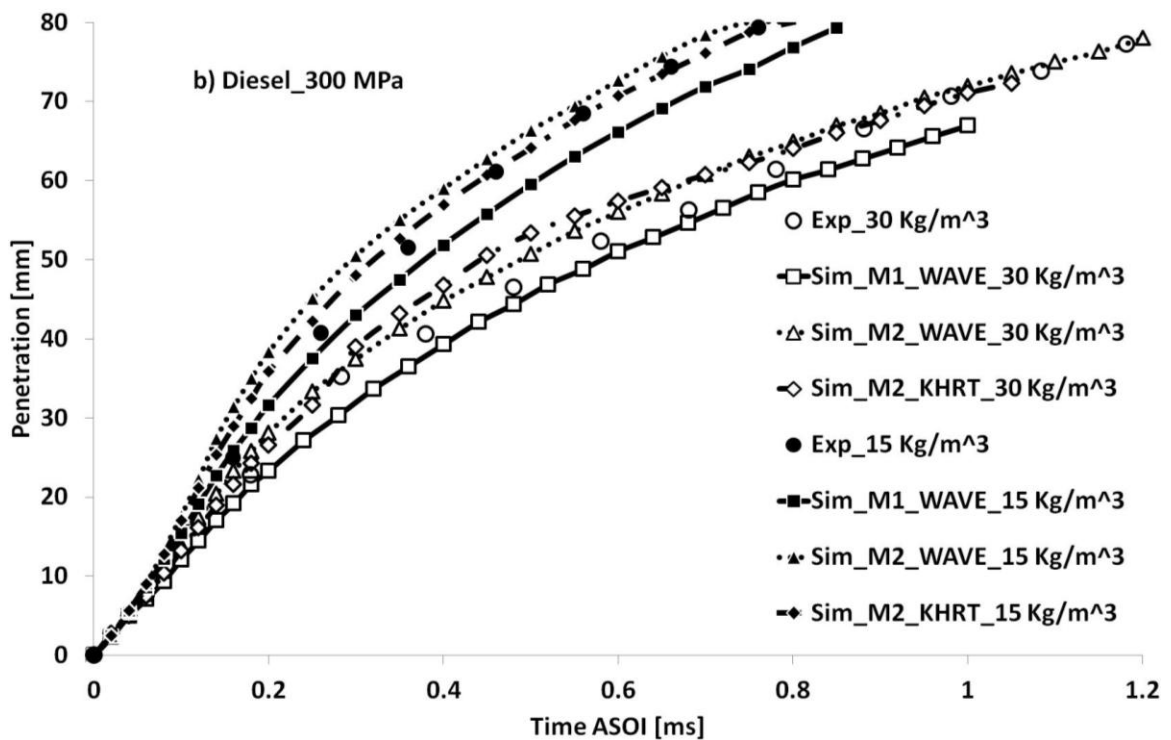
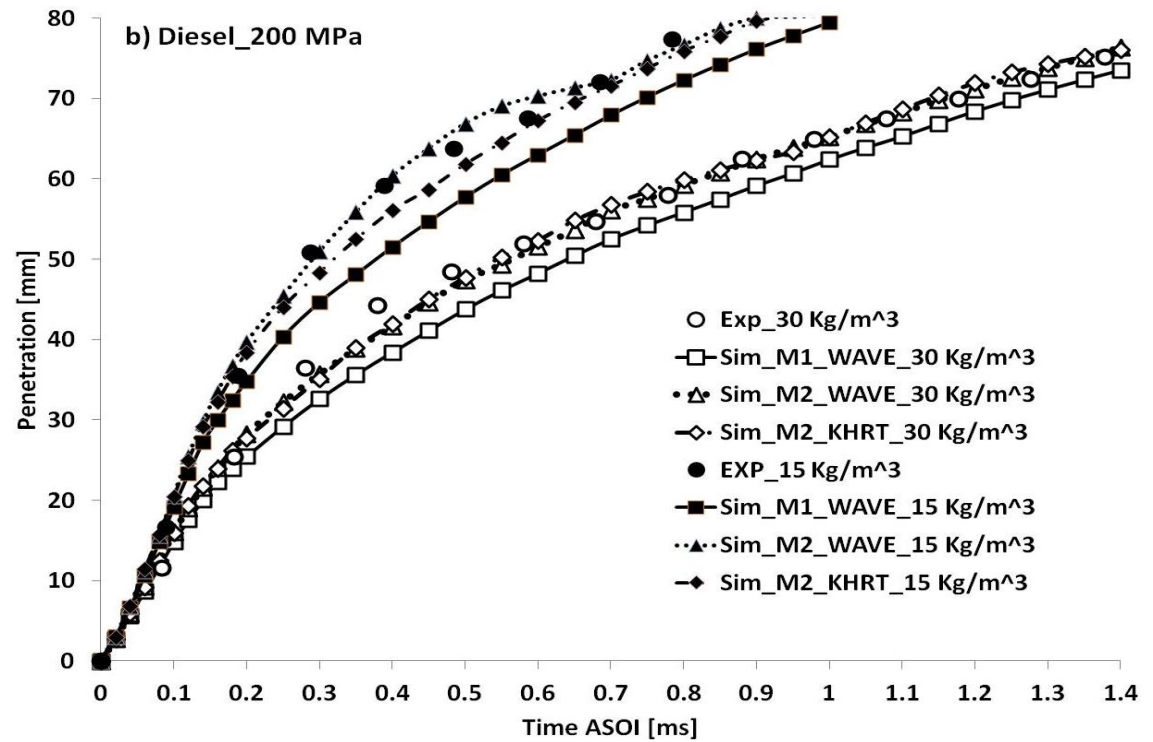
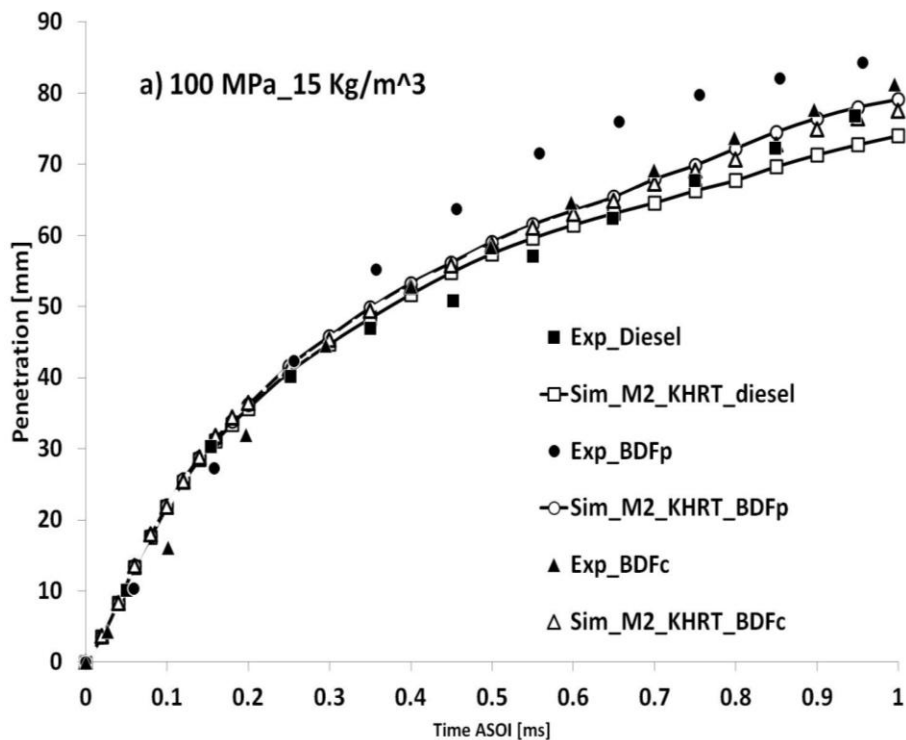


Figure 2.3: Effect of ambient density, mesh structure and break-up model on spray tip

penetration: a) 100 MPa; b) 200 MPa; c) 300 MPa

Influence of injection and ambient pressure, and fuel type on spray cone angle is presented in Fig. 2.5 for 0.7 ms after start of the injection (ASOI). The spray cone angle is defined as the angle between two lines starting from the nozzle tip through two points of maximum radial distance of the liquid parcels. Spray cone angle can be considered as a criterion for air entrainment into the fuel spray liquid core. Larger cone angle is usually accompanied by lower penetration, more successful break-up and faster mixture formation. As can be seen in Fig. 2.5, although in some cases increasing the injection pressure slightly increases the spray cone angle, it does not show much sensitivity to it. On the other hand, for the diesel fuel at higher chamber density, larger increase in the cone angle is observed. For the different fuel types, BDFp with largest surface tension and penetration has the smallest spray cone angle. The largest values of cone angle occur for the diesel fuel having the lowest surface tension and penetration.



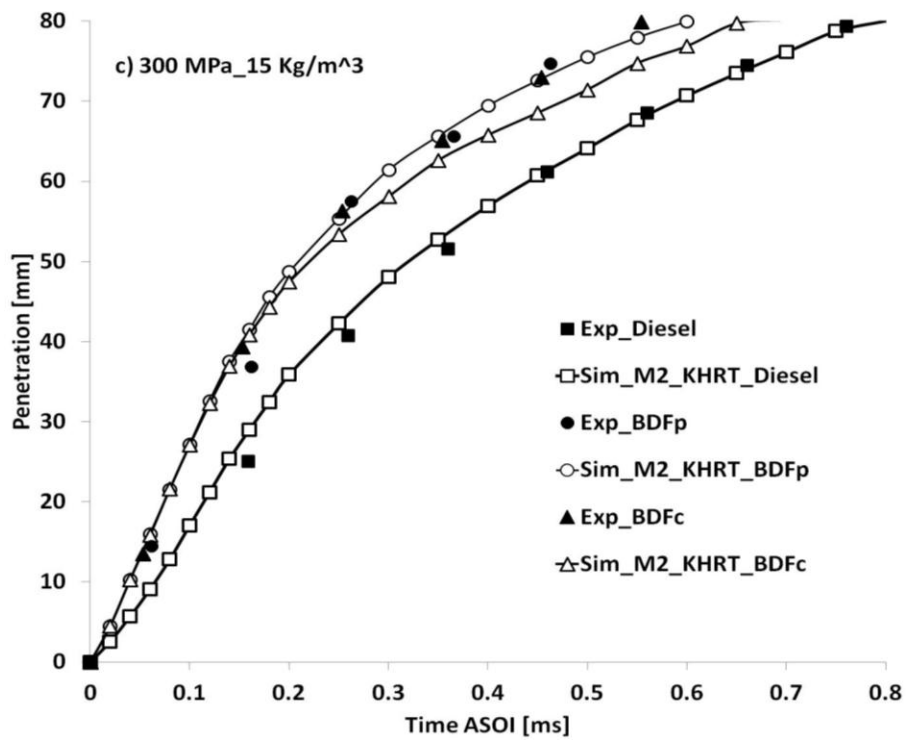
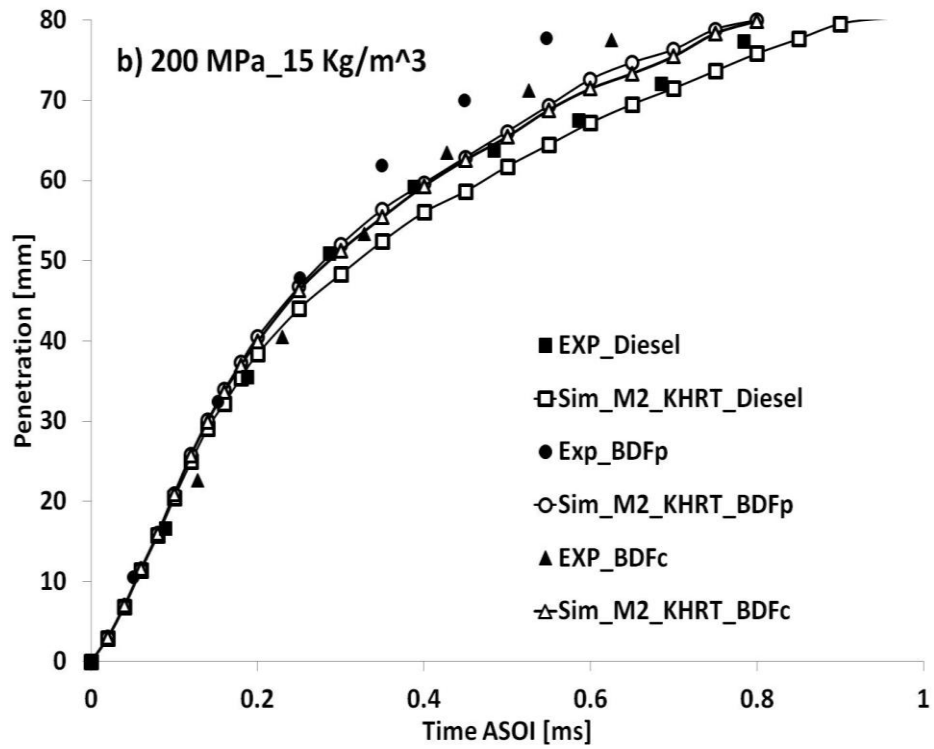


Figure 2.4: Influence of fuel type on spray tip penetration: a) 100 MPa; b) 200 MPa; c) 300 MPa

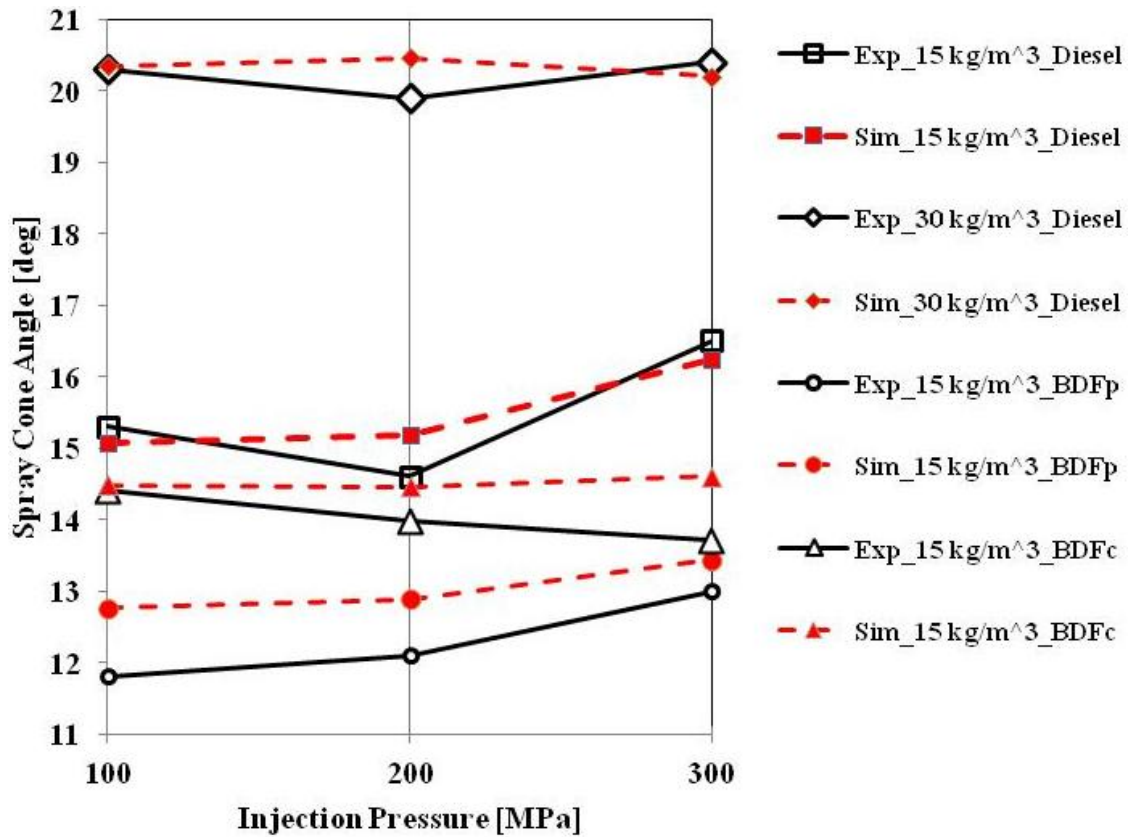


Figure 2.5: Variation of spray cone angle with injection pressure

Fuel volume fraction contours at the central plane of the spray, superimposed with the droplet particle cloud, are illustrated in Fig. 2.6 for different injection pressures at the density of 15 kg/m^3 . As can be seen from this figure, spray conical shape, cone angle, droplet penetration and radial dispersion are in good agreement with the experimentally captured images for all of the cases. In addition, the superimposed contours portray a dense liquid core extending from the nozzle, up to a distance at which the disintegration of the core occurs. In the case of the highest injection pressure of 300 MPa, the intact core extends further for BDFp. This is due to the high surface tension and viscous forces which inhibit liquid disintegration.

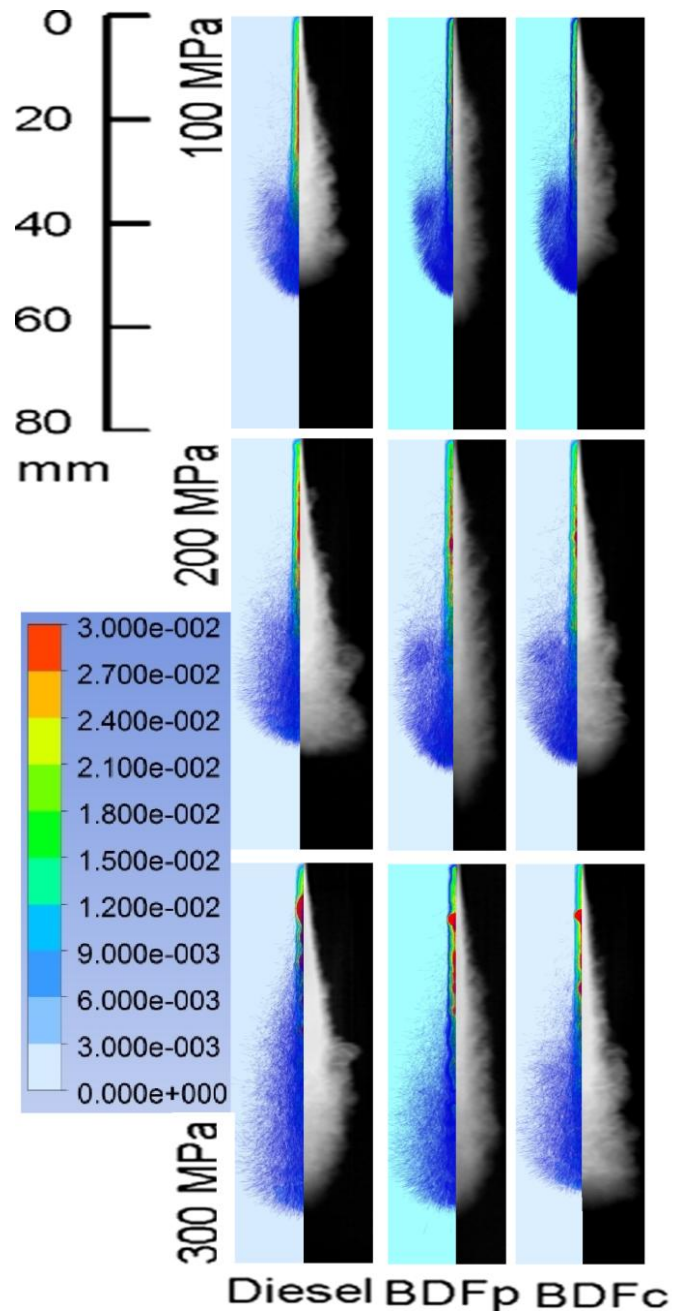


Figure 2.6: Comparison of experimental (Wang et al., 2010) images and simulated droplet cloud superimposed with fuel volume fraction contour at the central plane of the spray at 0.45ms ASOI

2.3.2 Sauter mean diameter (SMD)

The effect of injection pressure and ambient density on Sauter Mean Diameter of the diesel fuel is shown in Fig. 2.7. Sauter Mean Diameter ($SMD = d_{32} = \frac{\sum_{i=1}^m d_i^3}{\sum_{i=1}^m d_i^2}$) is a global description of the diameter of a drop whose volume-to-surface ratio is equal to that of a group of droplets with diameters d_i . It is defined as the summation of the volume of all droplets (which is constantly increasing with the injection of the new blobs) divided by the summation of the surface area of all droplets (which increases due to the droplet break-up). Immediately after injection, the SMD value is equal to the blob size injected, but for high pressure injection sprays it dramatically decreases due to the atomization of the droplets. The rate of this reduction is higher in the largest injection pressure of 300 MPa due to the diminution of the break-up time associated with the increased Weber number. On the other hand, higher chamber densities are tied in with a lower rate of SMD reduction and slightly higher values of SMD at the final stage of the SMD calculation. Since there is no experimental data, results are compared with the analytical correlation suggested by Ejim et al. (2007) for diesel and biodiesel fuels. Increased ambient density and reduced ΔP_{inj} lead to higher SMD prediction. But it can be seen that injection pressure has more effect on SMD in comparison to ambient density. The SMD [μm] correlation is as follows:

$$SMD = 6156\nu^{0.385}\sigma^{0.737}\rho_f^{0.737}\rho_a^{0.06}\Delta P^{-0.54} \quad (13)$$

where ν [m^2/s] and σ [N/m] are viscosity and surface tension, ΔP [bar] is the difference between injection and ambient pressures, ρ_f and ρ_a [kg/m^3] are fuel and ambient density respectively.

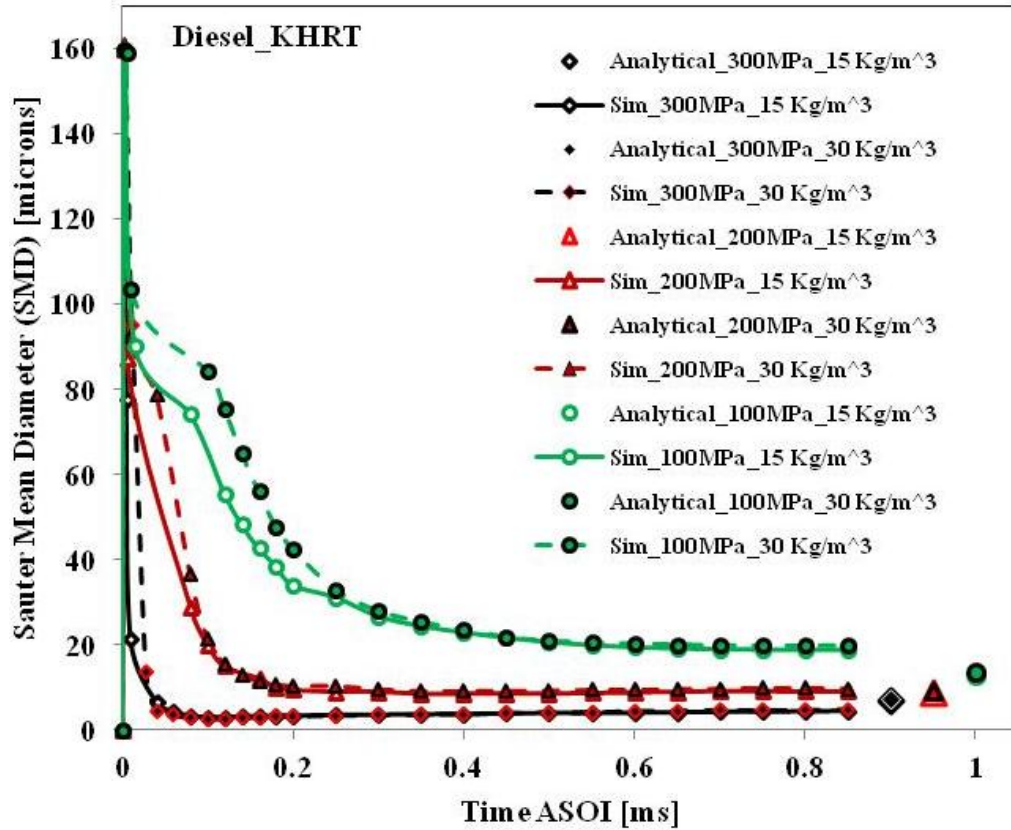


Figure 2.7: Effect of injection pressure and ambient density on SMD in diesel fuel spray

The effect of fuel type on SMD is shown in Fig. 2.8, compared again to the analytical results based on equation (13). In the larger SMD formation of the biodiesel fuels observed here, kinematic viscosity, surface tension and density play the major role. The surface tension force attempts to keep the droplet unbroken by opposing the aerodynamic forces, while the viscous force serves as a damper against the perturbations created at the droplet surface leading to the postponement of the break-up. This is observed in Fig. 2.8 where BDFp with largest surface tension and kinematic viscosity provides for larger SMD and a slower break-up rate.

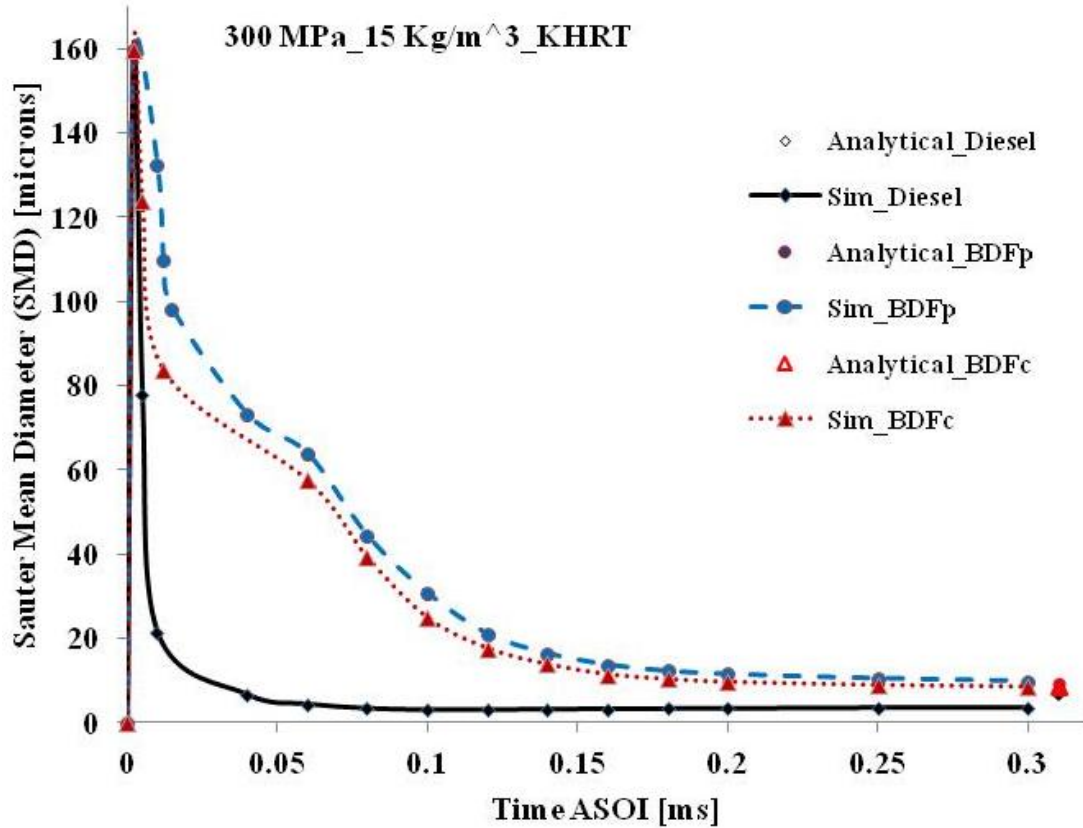


Figure 2.8: Effect of fuel type on SMD

2.3.3 Droplet Temporal and Spatial Size Distribution

Although Sauter Mean Diameter (SMD) gives some clues about the jet break-up, it is beneficial to carry out a local and temporal droplet size distribution analysis. A plot of 315,710 droplet diameters of BDFp at 300 MPa injection pressure, 15 $[kg/m^3]$ ambient density at 0.6 ms after start of injection is depicted in Fig. 2.9. In region (I), most of the droplets close to the nozzle and near the spray core have diameters close to the nozzle size while in region (III), which is also close to the nozzle exit, droplets located at the shear layer of the jet are atomized faster due to the more aerodynamic interaction with the gas. In region (II) at a distance between 10-15 mm away from the nozzle exit, a large number of the droplets break-up into smaller ones. As can be seen in region (IV), due to

the high injection pressure up to the current time (0.6 ms), most of the droplets have broken up. In region (V) a small number of the droplets could be detected with diameters larger than nozzle size. These droplets are the ones which have been coalesced due to collision, and travelled further downstream in the chamber.

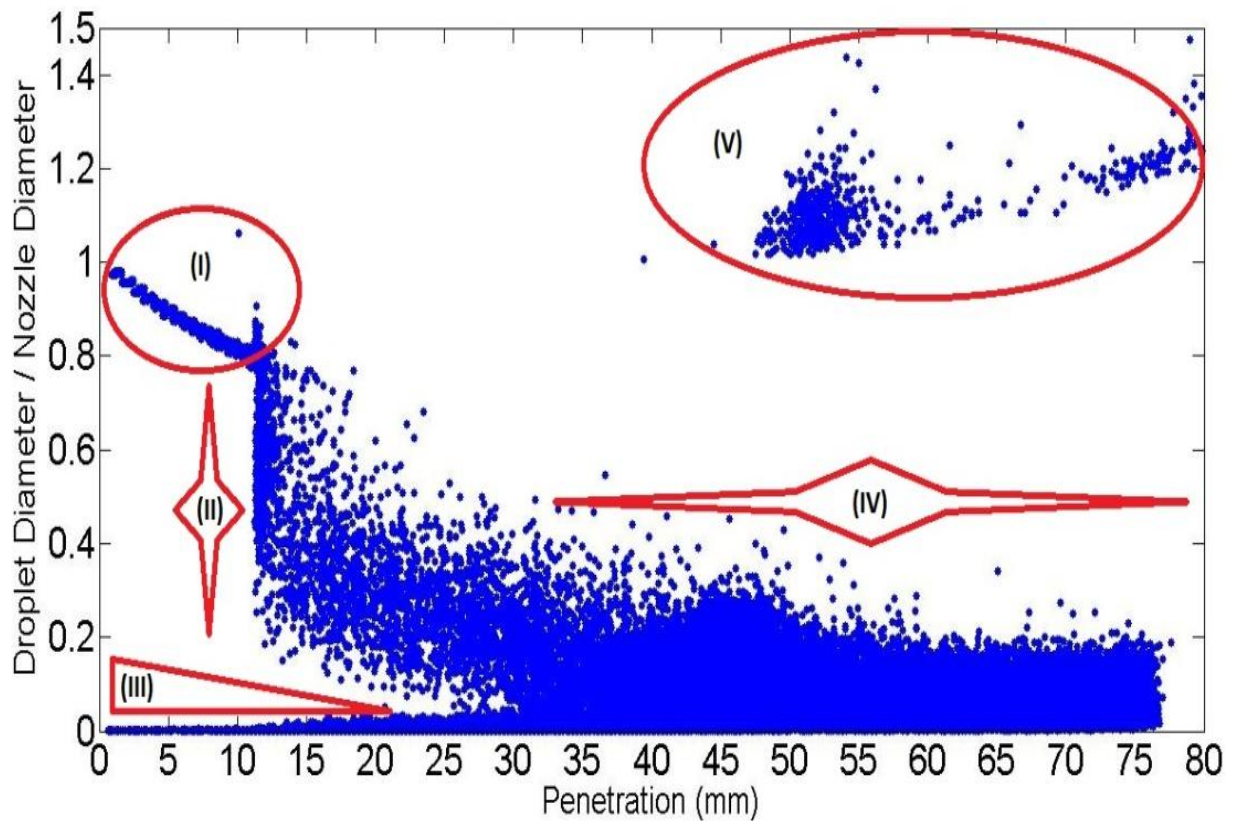
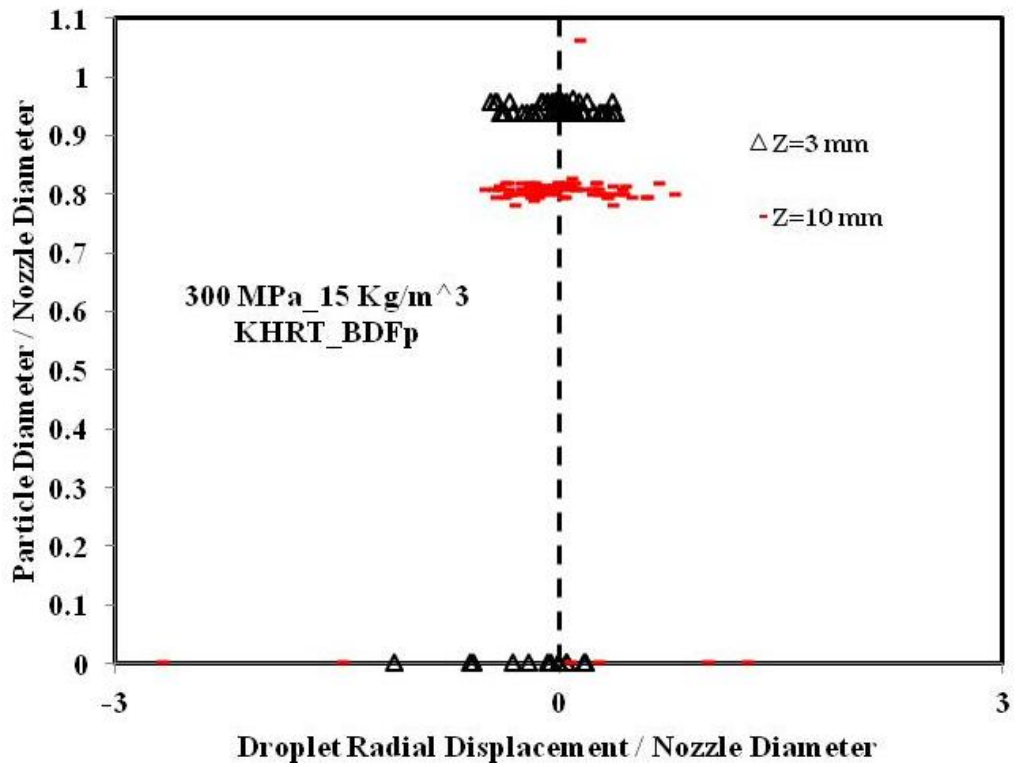


Figure 2.9: Droplet diameter normalized by nozzle diameter vs. droplet penetration

Radial droplet size distribution for BDFp on the planes defined normal to the spray axis at different axial locations ($Z = 3, 10, 20, 40, 50, 70$ mm) with an injection pressure of 300 MPa and ambient density of $15 \text{ [kg/m}^3\text{]}$ is represented in Fig. 2.10. At $Z = 3$ mm and $Z = 10$ mm, droplets have almost a uniform radial size distribution and, except for a few, most of them are of a size very close to the nozzle size. For the $Z = 20$ mm, although the droplet size has become slightly smaller, a uniform radial size distribution persists. At $Z =$

40 mm, more break-up has occurred at the periphery of the spray, while close to the axis larger droplets are observed in the dense core of the jet. At $Z = 50$ mm and $Z = 70$ mm, most of the droplets have broken up in both the central and exterior spray regions due to a fully dispersed jet and high level of ambient air entrainment. A small number of coalesced droplets are also observed at $Z = 70$ mm which have been able to penetrate farther downstream into the ambient region.



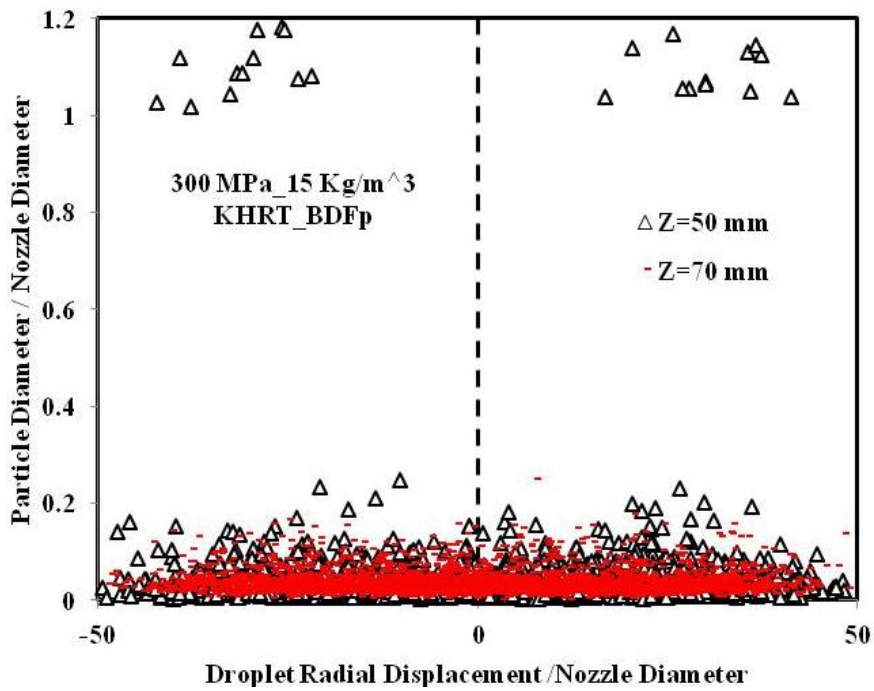
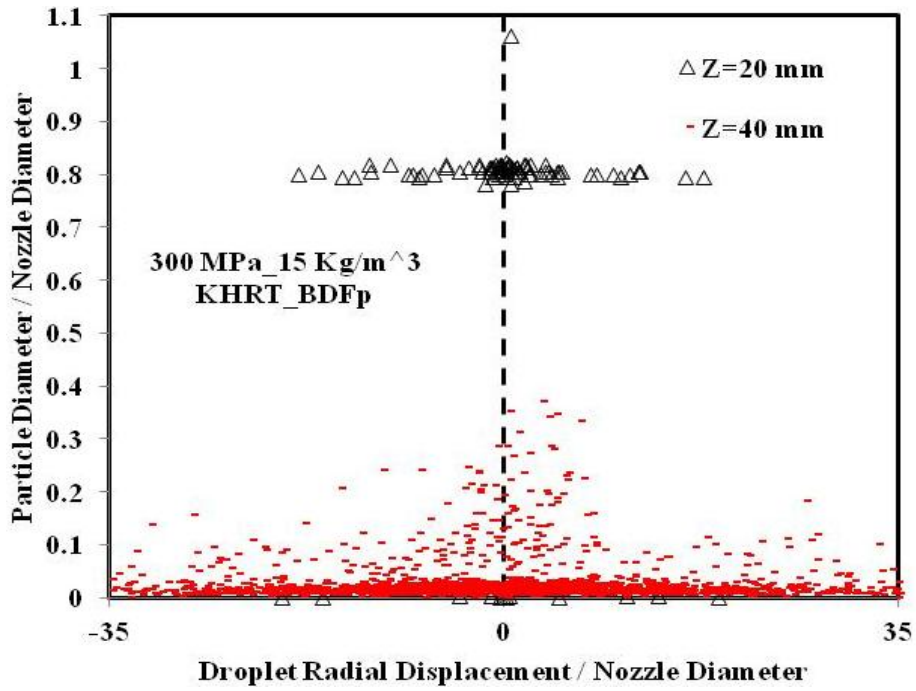


Figure 2.10: Radial distribution of particle size on different planes normal to the spray axis

In order to study the temporal size distribution of the droplets, a histogram of droplet size is provided at certain times ($t = 0.01, 0.02, 0.06, 0.07, 0.1, 0.2, 0.4, 0.6$ ms) after the start of injection, which is shown in Fig. 2.11. At earlier time periods, the probability of occurrence of large droplets is high. The single peak at $t = 0.01$ ms suggests that most of the droplets have a size close to the nozzle diameter. Following this, the number of larger particles decreases and the number of smaller particles increases due to the break-up. During the times $t = 0.02 - 0.1$ ms, a bimodal size distribution of the droplets is observed. At later times while the peak is moving to the left, the small droplets dominate up to the time $t = 0.6$ ms, at which the number of large particles becomes insignificant. A small percentage of coalesced particles is observed at times $t = 0.06, 0.07, 0.1$ ms, but these droplets vanish at later times.

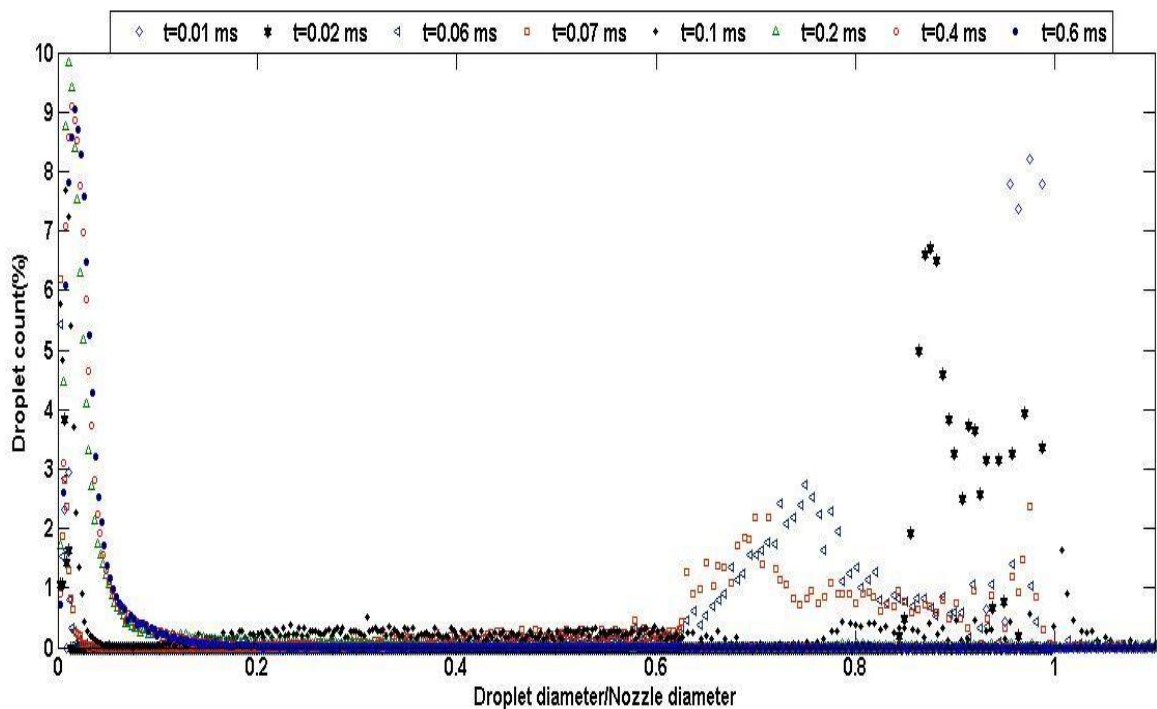


Figure 2.11: Droplet size histograms

2.4 Conclusions

In this chapter, the spray behaviour and characteristics of ultra-high injection diesel fuel, palm oil (BDFp) and cooked oil (BDFc) as biodiesel fuels have been studied. Numerical results have been validated using the experiments of Wang et al. (2010) in a constant volume chamber. The influence of injection and ambient pressure, fuel type and mesh structure on the spray penetration have been investigated and compared to experiments.

For all the cases, an increase in the injection pressure caused an increase in spray penetration, however, the penetration decreased in the presence of higher ambient density. Biodiesel fuels yield more penetration and larger SMD in comparison with diesel fuel. This encourages the application of ultra-high injection pressures in biodiesel fuels to facilitate their atomization by overcoming their high surface tension and viscous forces resisting their disintegration.

The spray cone angle was compared with experiments at a certain time after the start of the injection, showing its higher sensitivity to ambient density rather than injection pressure. In addition, the smaller spray cone angle of the biodiesels confirms their lower rate of expansion and atomization compared with diesel fuel.

Study of the Sauter Mean Diameter (SMD) variation with time for different injection and ambient pressures, and also various fuel types, revealed the fact that all the fuels atomize faster in the presence of higher injection pressures and slightly slower in higher ambient densities. It was also observed that biodiesels break-up slower than diesel fuel.

Droplet size distribution and probability density function analysis was carried out in order to achieve an understanding of the temporal and spatial droplet size variation.

Break-up regions, locations and times of atomization can be distinguished, and coalesced particles were detected for the BDFp fuel.

CHAPTER 3

Spray-to-Spray Collision Break-up of Ultra-High Injection Pressure

Diesel Fuel

3.1 Introduction

The extensive range of applications and the inherent multiphase phenomena taking place in sprays have made them interesting and important flows for both industrial and academic studies. In direct injection diesel engines, optimization of the sprays contributes significantly to high efficiency and low emission combustion.

Ambient flow conditions like pressure (Roisman et al., 2007), and temperature (Park et al., 2010), and combustion chamber flow field structure (Ghasemi & Djavareshkian, 2010), influence spray formation and development and consequently the mixture formation in the chamber. In order to achieve higher levels of atomization to enhance the mixture formation, ultra-high injection of the sprays has been implemented, taking into account fuel type, (Ghasemi et al., 2012) and chamber geometry effects (Fukuda et al., 2012). The effect of different classical and hybrid break-up models on the spray formation and break-up has also been investigated (Djavareshkian & Ghasemi, 2009).

There have also been some studies on interacting sprays. Collision processes play a major role in spray-to-spray interactions. Since the conventional O'Rourke collision model only considers a bounce and a coalescence of the same kind of droplets (water-water or fuel-fuel), other researchers have made attempts to develop new collision models which account for multi-

species interaction (Tsuru et al., 2010). It has also been shown that interacting sprays can contribute to atomization by causing a reduction of Sauter mean diameter (SMD) compared to single sprays (Arai & Saito 1999). The spray volume increases significantly due to the interaction of the sprays. Increasing the spray angle leads to a reduction in droplet velocities. On the other hand, impingement distance does not have a major influence on the droplet velocities since it is related to the travelling distance of the droplets (Ko & Ryou, 2005).

The objective of this work is to study the collision breakup process of two interacting fuel sprays. A single spray injected into an initially quiescent constant volume chamber is first simulated using the Eulerian-Lagrangian approach. Reynolds-Averaged Navier-Stokes equations, with the $k - \varepsilon$ turbulence model, are solved using an Eulerian formulation for the continuous phase. The droplet discrete phase is treated using a Lagrangian formulation together with spray sub-models. The single spray results are validated against experimental data of Wang et al. (2010). Then, the influence of incidence angle and separation distance between the two interacting sprays on the spray parameters like tip penetration, Sauter mean diameter and spray cone angle is investigated. Spray tip penetration is redefined based on the temporal development of the tip of the merged spray.

3.2 Numerical Methodology

3.2.1 Computational Modeling

The Eulerian-Lagrangian multiphase approach is adopted in order to calculate the interaction of the discrete (fuel) and continuous (air) phases. The Eulerian formulation defines the related fluid flow parameters such as velocity components, pressure, density and temperature as a function of position (x,y,z) and time t for the entire three-dimensional flow domain, at each time

step (1×10^{-6} sec for this case). The Reynolds Averaged Navier-Stokes (RANS) equations are solved for the continuous phase using the standard $k - \epsilon$ turbulence model. These equations are spatially discretized by the finite volume method, using the QUICK algorithm for the convective terms in momentum and turbulence equations, and the STANDARD scheme for pressure interpolation. A fully implicit first-order scheme is used for the temporal discretization. The pressure-velocity coupling in the discretized equations is performed using the SIMPLEC algorithm. All the surfaces of the domain are considered as no-slip walls. No inlet and outlet boundary conditions are defined for the Eulerian phase. For the Lagrangian phase the discrete phase inlet condition is defined as a nozzle area around an injection point where the liquid blobs are injected into the chamber.

In the Lagrangian approach, each droplet is considered as a single mass particle, the velocity of which is decelerated by aerodynamic interaction of the gas and droplet, and the mass of which is decreased by evaporation, etc. The two phases continuously exchange momentum, energy and mass. These exchanges are accounted for by applying source terms in the conservation equations of the gas phase in each grid cell. On the other hand, the gas phase affects the dispersed liquid phase by employing the local values of temperature, gas velocity etc., of the grid cell through which the droplet is passing at each time step as a boundary condition (Baumgarten, 2006).

3.2.2 Grid Generation and CFD Tool

The CFD simulations have been performed using ANSYS FLUENT 13 by modeling diesel spray injection into a constant volume chamber of size $60 \times 60 \times 80 \text{ mm}^3$. The mesh generation process included running simulations on several different fully structured meshes containing from 5×10^5 to 1.8×10^6 cells to acquire grid independent results. Figure 3.1

shows the predicted time evolution of the spray tip penetration on several grids after start of injection (ASOI). Clearly, the 5×10^5 mesh is too coarse to capture the spray penetration, and the results converge as the mesh is refined, with the final two meshes showing essentially no difference. Based on the results displayed in this figure, the mesh with 1.44×10^6 cells was selected for subsequent calculations.

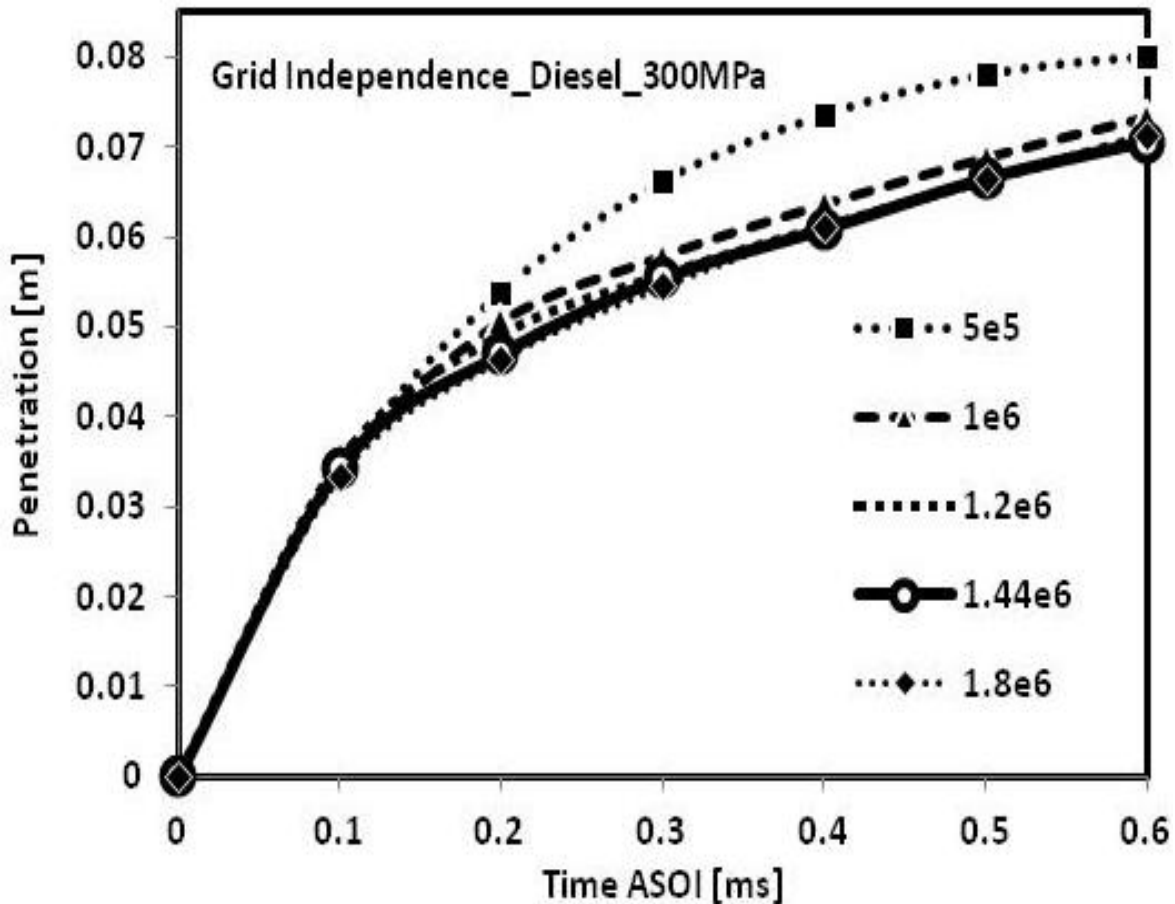


Figure 3.1: Grid independence tests

3.2.3 Spray Sub-models

For the fuel spray simulations, different sub-models are implemented to account for the effects of turbulent dispersion (Gosman & Ioannides, 1981), coalescence (Ashgriz & Poo, 1990), evaporation (Faeth, 1983), droplet breakup (Wierzba, 1993) and collision (O'Rourke, 1981).

3.2.4 O'Rourke Collision Model

The standard collision model usually implemented in conventional spray simulations is the O'Rourke model (O'Rourke, 1981), which only allows for permanent coalescence and stretching separation in droplet collisions. Based on an energy balance, it is determined whether the coalesced droplets would separate again to re-form the initial drops, or merge to create a larger droplet. Stretching separation occurs if the rotational energy of the coalesced drops,

$$E_{Rot} = \frac{L^2}{2J} \quad (14)$$

is larger than the extra surface energy,

$$\Delta E_{Surf} = 4\pi\sigma(r_1^2 + r_2^2 - r_{eff}^2) \quad (15)$$

Otherwise, permanent coalescence will occur. In these equations L , J , r_1 , r_2 , r_{eff} are respectively angular momentum about the centre of mass of the coalesced droplet, the corresponding moment of inertia, radii of the colliding droplets and the effective radius, given by

$$L = \frac{m_1 m_2}{m_1 + m_2} u_{rel} X \quad (16)$$

$$J = \frac{2(m_1 + m_2)}{5} r_{eff}^2 \quad (17)$$

$$r_{eff} = (r_1^3 + r_2^3)^{1/3} \quad (18)$$

where m_1 , m_2 and X are the droplet masses and the off-centre distance respectively. Transition between coalescence and stretching separation is a function of the collision Weber number

$$We_{coll} = \frac{\rho_l d_2 U_{rel}^2}{\sigma} \quad (19)$$

and the drop diameter ratio, where ρ_l , d_2 , U_{rel} and σ are the fuel density, smaller droplet diameter, relative collision velocity and surface tension, respectively.

3.2.5 Injection and Nozzle Properties

In these simulations diesel fuel was injected into the constant volume chamber from a single hole 160 μm diameter nozzle with a nozzle hole length-to-diameter ratio of 7.5. Fuel injection pressures up to 300 MPa were applied into the quiescent ambient air with density 15 Kg/m^3 corresponding to 1.27 MPa. Fuel properties taken from Wang et al. (2010) are shown in Table 3.1. The injector geometry and the variable mass flow rate profile applied to the simulations are shown in Fig. 3.2.

Table 3.1 Fuel properties (Wang et al., 2010).

Fuel type	Diesel
Density ($\frac{Kg}{m^3}$) @ 15 °C	830
Viscosity ($\frac{mm^2}{s}$) @ 30 °C	3.36
Surface tension ($\frac{mN}{m}$)	25.5
Cetane Number	55
Heating value ($\frac{MJ}{Kg}$)	43.1

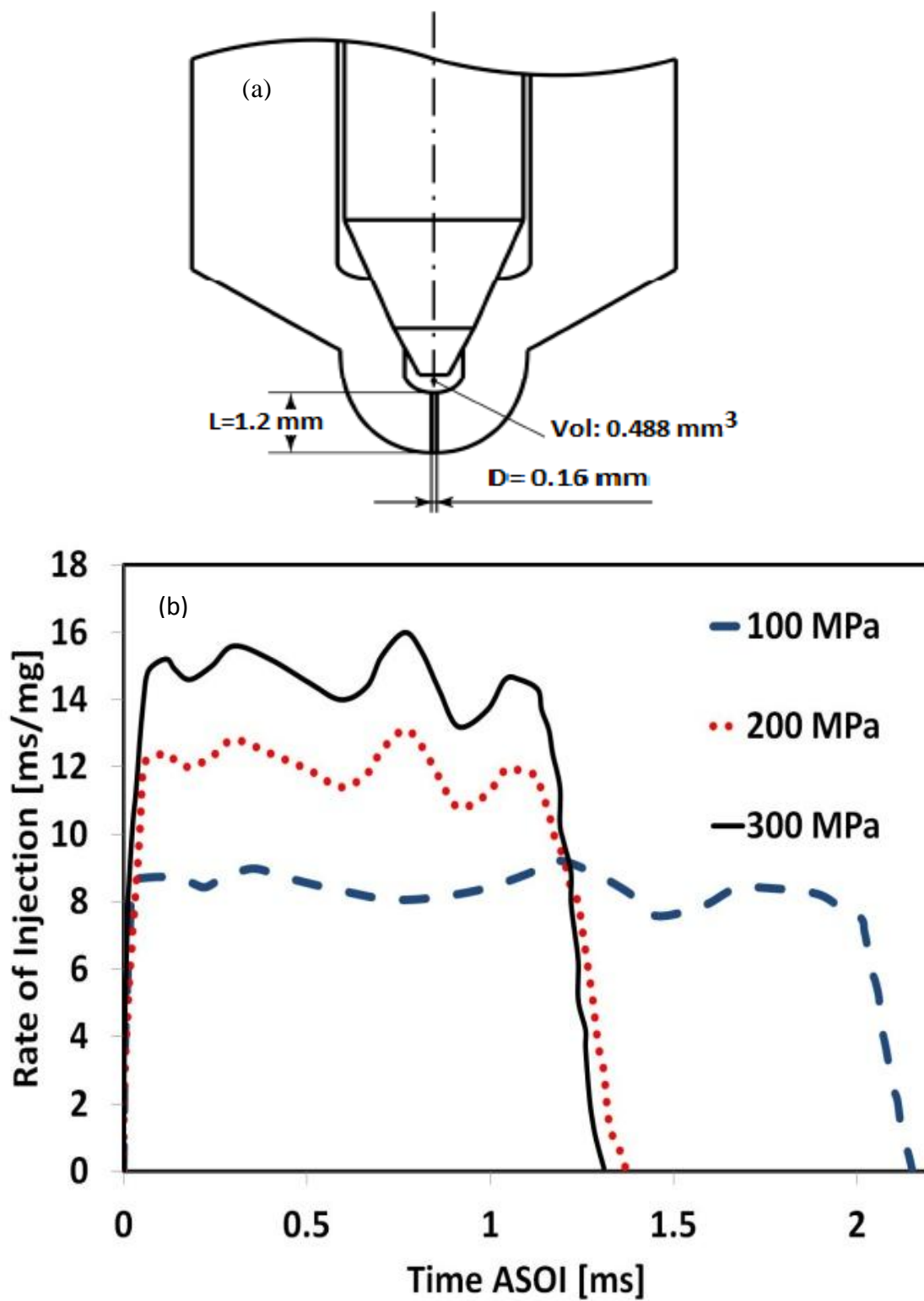


Figure 3.2: (a) Nozzle geometry, and (b) injection mass flow rate profile vs. injection time

(Wang et al., 2010)

3.3 Results

3.3.1 Single Spray

Simulation results for a single spray are discussed in this subsection. These results correspond to the diesel fuel case for a single spray that was investigated in Chapter 2. Figure 3.3 shows a comparison of the simulated single spray droplet cloud superimposed with contours of liquid fuel mass fraction in the jet central plane to experimentally captured images, for injection pressures of 100, 200 and 300 MPa. As can be seen, the simulated spray expansion and penetration for all injection pressures both match very well with the experimental images.

Figure 3.4 displays predicted spray tip penetration compared to experiments. As this figure illustrates, a higher injection pressure leads to a higher penetration of the spray tip into the ambient air. The spray penetration starts with a near linear trend and takes an asymptotic shape due to the aerodynamic deceleration caused by the ambient fluid. Again, there is very good agreement between the simulation results and the experimental measurements,

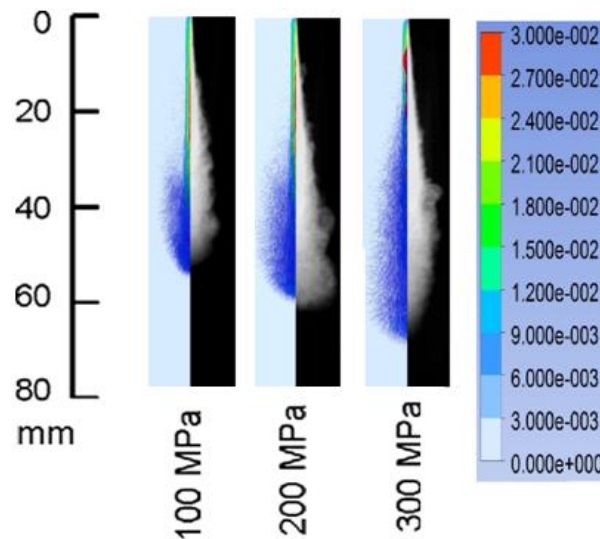


Figure 3.3: Comparison of experimental (Wang et al., 2010) images and simulated droplet cloud superimposed with fuel volume fraction contour at the central plane of the spray at

0.45ms ASOI

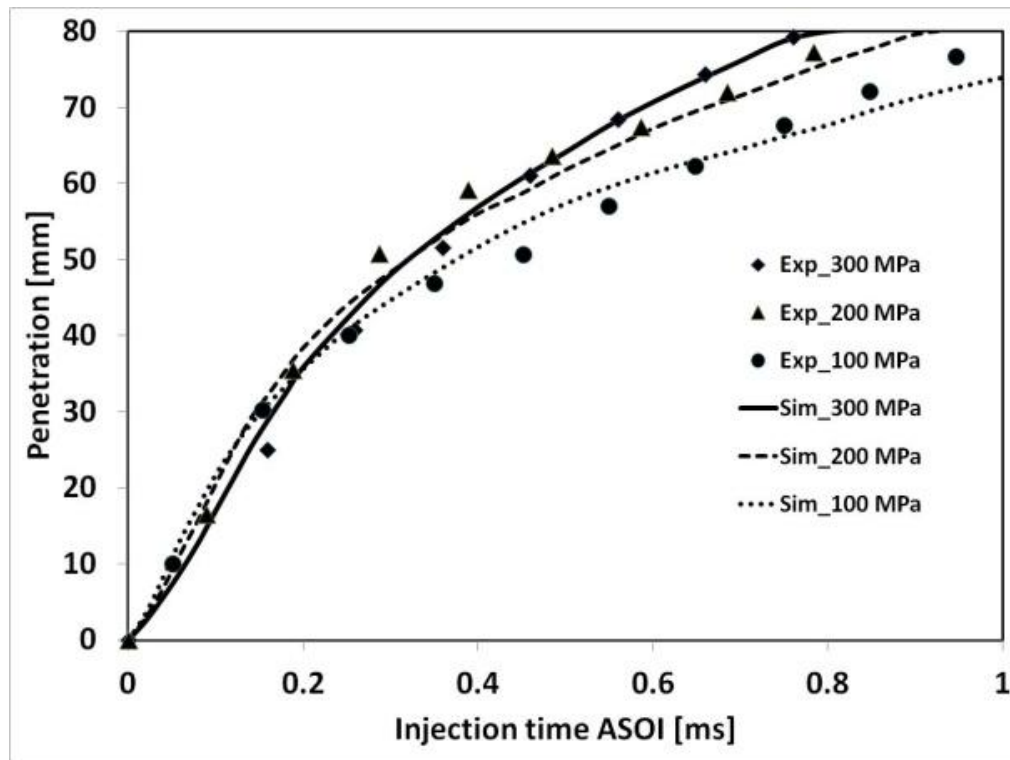
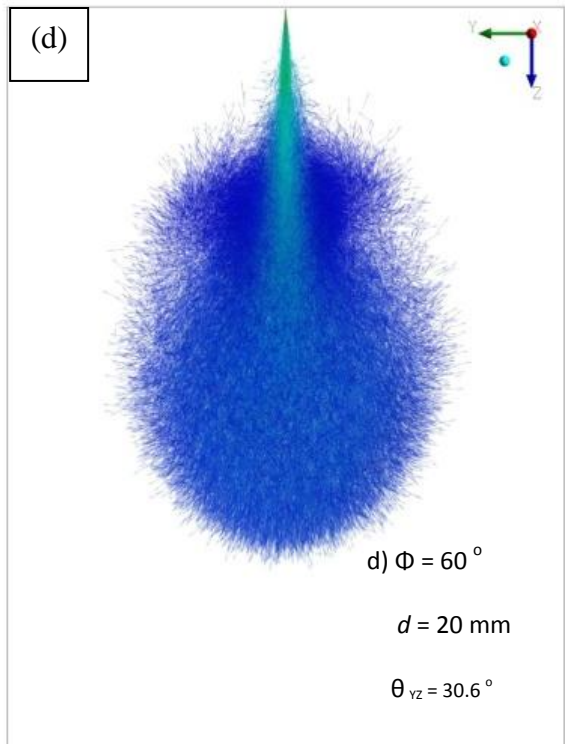
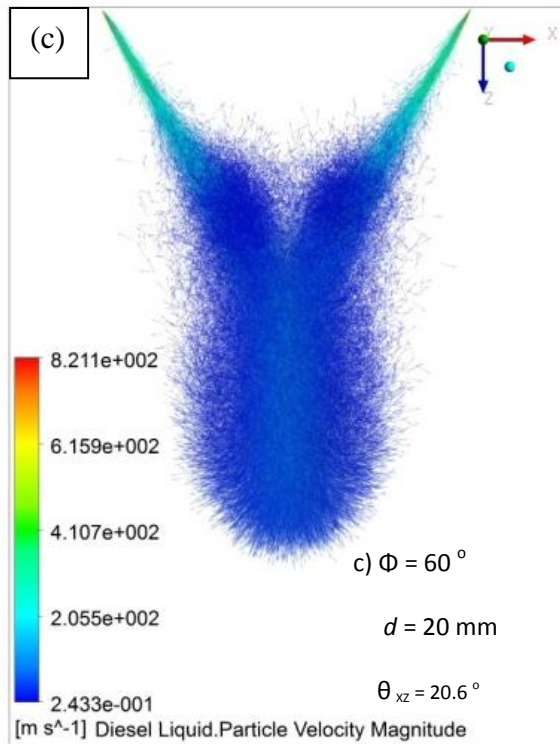
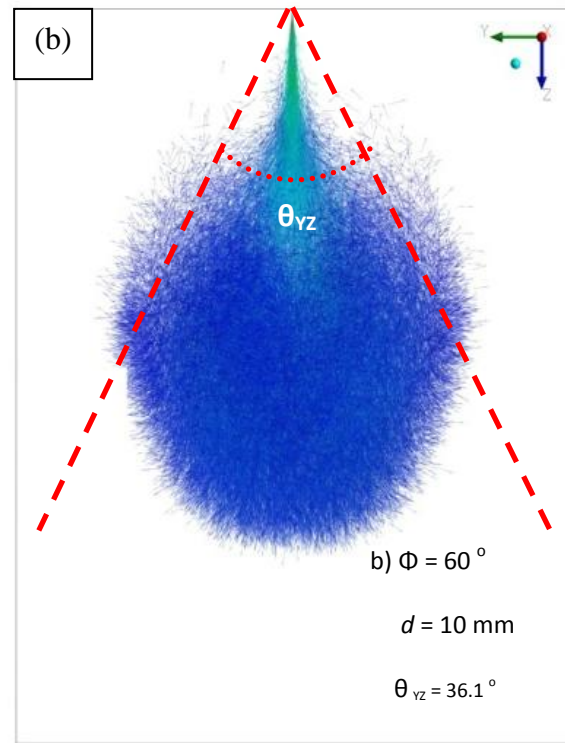
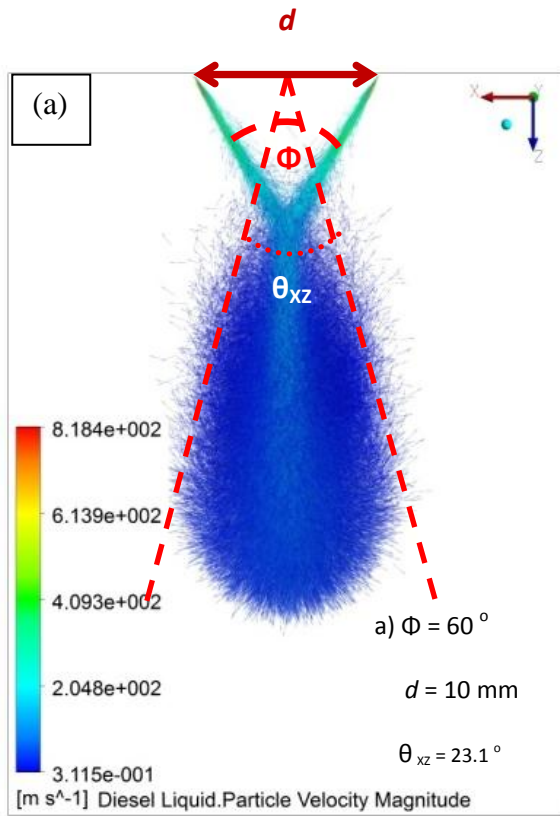


Figure 3.4: Spray tip penetration; simulation (Sim) vs. experiments (Exp), (Wang et al., 2010)

3.3.2 Merging Sprays

In this section flow features of two merging sprays are investigated. Effect of incidence angle and injection location distance on the merged spray parameters such as cone angle, penetration and SMD are studied. Two injection location distances of $d = 10, 20$ mm and incidence angles of $\Phi = 60, 90$ are considered. Figures 3.5a-h illustrate images of the particle cloud colored by droplet velocity magnitude of the two merging sprays at $t = 1$ ms. In these figures, $d, \Phi, \theta_{XZ}, \theta_{YZ}$ are nozzle distance, spray incidence angle, and merged spray cone angle in the XZ and YZ planes, respectively. Spray pairs are injected in the XZ plane. However, for all the cases, the spray expansion is greater in the YZ plane ($\theta_{YZ} > \theta_{XZ}$) than in the XZ plane. Before impingement of the sprays which are injected in XZ plane, droplets have velocity components in XZ and YZ planes. Velocity components in the X direction are cancelled out and subjected to more dissipation. On the other hand, velocity component in the Y direction add up and

expand the merged spray in YZ plane. This high expansion of the spray provides an increased entrainment of the ambient air leading to a more successful mixture formation. It can be observed from these figures that increasing the nozzle separation distance (d) and reducing the spray incidence angle(Φ), decreases the merged spray cone angles in both XZ and YZ planes. This reduction is more significantly affected by the incidence angle, since incidence angle has a larger influence in collision relative velocity variation compared to the case of increasing the injection distance. Among the different cases studied, maximum cone angles ($\theta_{XZ} = 24^\circ$, $\theta_{YZ} = 48.4^\circ$) were observed in the case of $d = 10 \text{ mm}$, $\Phi = 90^\circ$ (Fig. 3.5e, f). This arrangement of the twin sprays is expected to provide an improved entrainment of the ambient air and a more effective mixture formation.



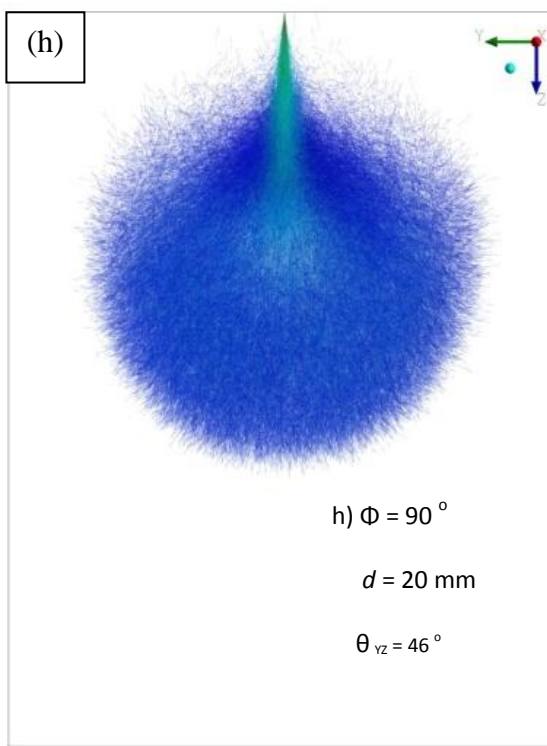
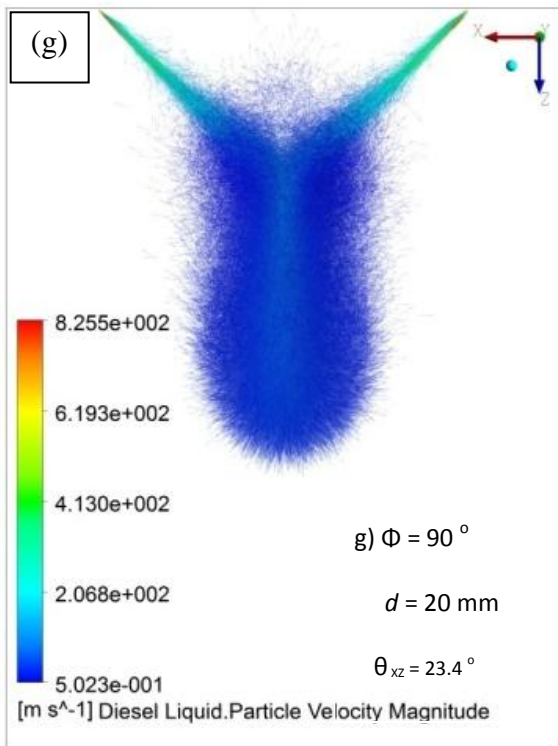
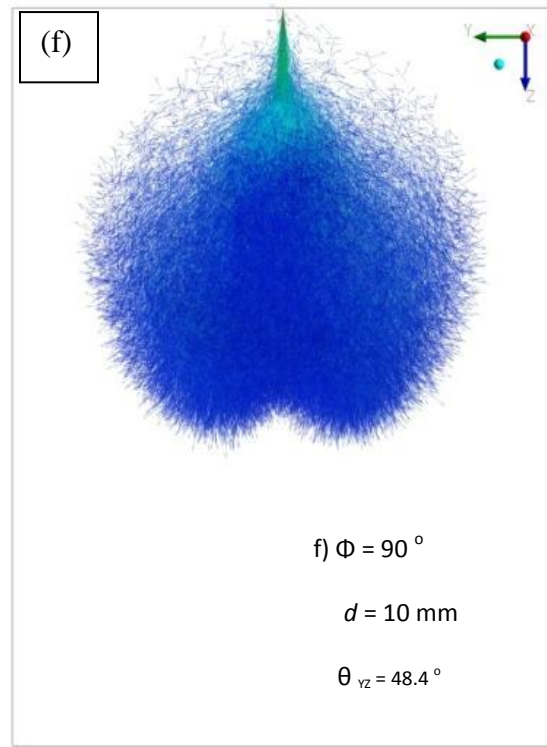
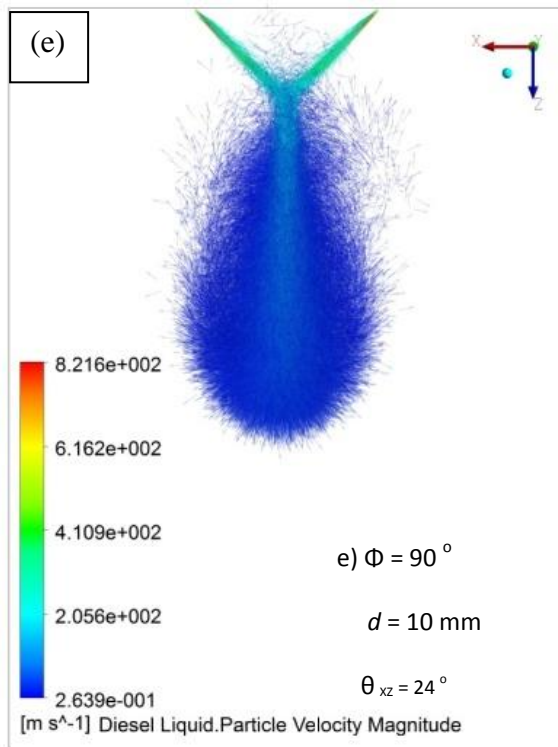


Figure 3.5: Droplet cloud of the merging sprays colored by velocity magnitude at $t = 1 \text{ ms}$

Figure 3.6 shows the temporal development of the merged spray into the ambient fluid. As can be seen from this figure, the merged spray penetrates significantly less distance into the ambient fluid compared to the single spray. Achieving higher levels of expansion and entrainment in a shorter distance could be a beneficial setup for small stroke IC engines, where wall impingement should be avoided. Increasing d leads to an increase in penetration while, conversely, increasing Φ results in a significant reduction in tip penetration. Increasing d affects the location, and only slightly affects the velocity of merging. Accordingly, penetration is somewhat larger. On the other hand, increasing the incidence angle from 60° to 90° increases the relative velocity of the collision which is in a direction normal to the merged spray axis. The increase in the relative velocity leads to a higher radial expansion of the spray and consequently lower penetration. This can be seen from the case of $d = 10 \text{ mm}$, $\Phi = 90^\circ$ (also see Figs. 3.5e,f), where the spray has maximum cone angles and minimum penetration.

Figure 3.7 shows the variation of Sauter mean diameter (SMD) with injection time. At the beginning of the injection the SMD is close to the nozzle size ($160 \mu\text{m}$) but, within the first 0.1 ms it sharply reduces as a result of the break-up. In this figure the SMD range has limited up to $8 \mu\text{m}$ to magnify the small SMD variations after this initial reduction. The O'Rourke model over-predicts coalescence (Lee et al., 2002) due to its inability to account for collision induced break-up (Ko & Ryou, 2005). The possible over-prediction in SMD also reported by Baumgarten (2006) is due to disregarding collision break-up in the O'Rourke model and augmenting coalescence instead. Although, in all the cases, break-up occurs in a very short time, twin sprays show higher SMD values as a result of the above-mentioned phenomena. Increasing d results in an increase in SMD, while

increasing Φ leads to a reduction. Larger droplets are more decelerated at the merging point, resulting in a lower relative collision velocity. On the other hand, at larger Φ , the relative collision velocity increases. Relative collision velocity is a major factor in determining the collision Weber number. According to Baumgarten (2006), at higher collision Weber numbers there is more likelihood for stretching or reflective separation of the collided droplets, and less chance for coalescence. This confirms the effects of changing d and Φ on the SMD variation, as illustrated in Fig. 3.7.

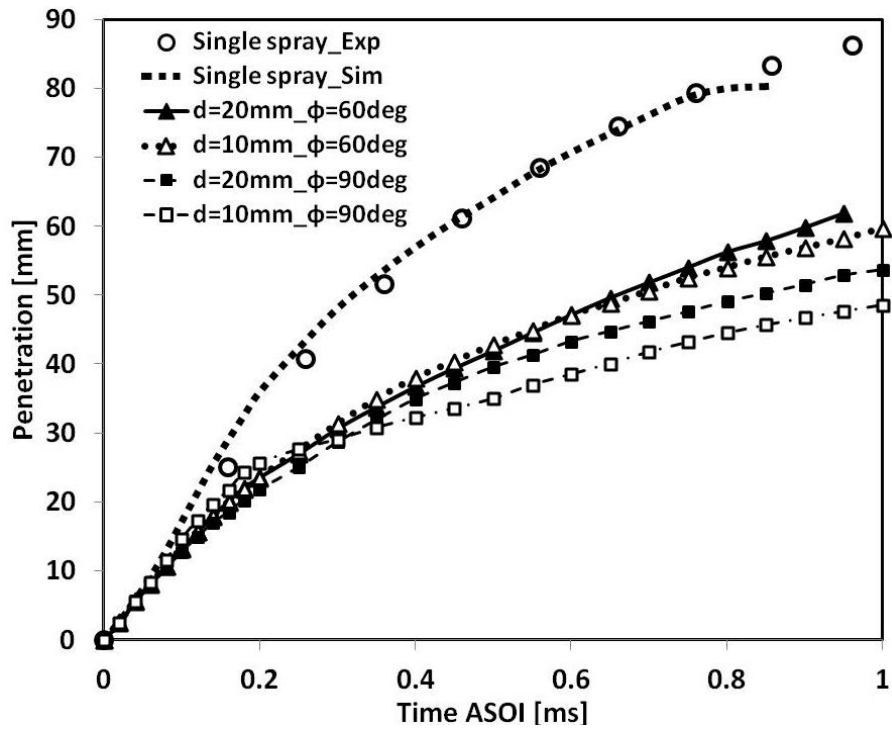


Figure 3.6: Comparison of spray tip penetration; simulation vs. experiments (Wang et al., 2010).

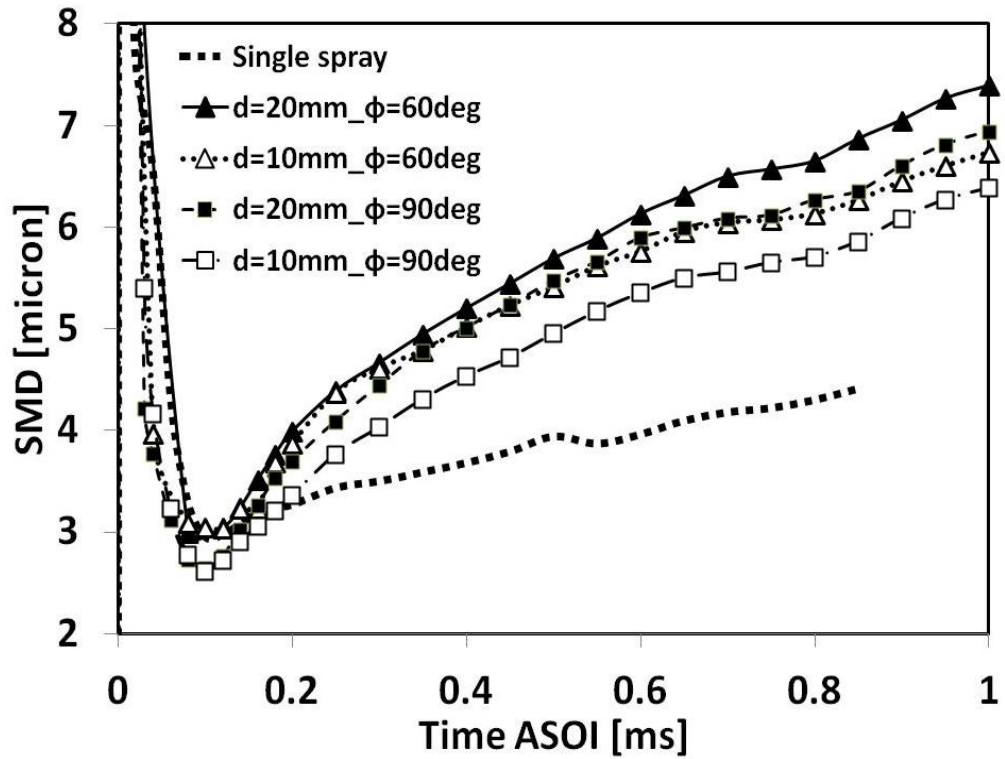


Figure 3.7: Sauter mean diameter (SMD)

3.4 Conclusions

In this chapter CFD simulations of single and interacting diesel sprays were conducted using the Eulerian-Lagrangian multiphase approach. Single spray results were validated against experimental data in terms of spray shape and penetration. The effects of incidence angle and nozzle separation distance on the collision of two merging sprays were studied. It has been shown that increasing nozzle separation distance results in an increase in merged spray tip penetration and SMD, while a reduction is observed in spray cone angle. In addition, increasing the incidence angle leads to reduction of the spray cone angle, penetration and SMD. For the cases considered, minimum SMD and penetration and maximum cone angle were observed in the case of sprays at right angles

to each other and 10 mm apart. This set-up could provide more advantages for the purpose of mixture formation due to its more successful atomization and higher spray expansion (entrainment) in a shorter penetration.

CHAPTER 4

Air Motion and Entrainment Analysis of Flow Induced by the Liquid Dispersion

4.1 Introduction

Quality of the fuel/air mixture inside the combustion chamber of a diesel engine is highly affected by the relative motion of the liquid and gas. In a low swirl or a quiescent combustion chamber the air motion is mostly induced by the liquid motion. Roll-up of the liquid jet shear layer engulfs the stagnant ambient air inside the spray. In addition, the momentum transfer from the liquid droplets to the gas forces the air into motion. Higher air motion results in more mixing. The level of air motion depends on the injection, ambient and sprays conditions.

In gaseous jets it is not too complicated to evaluate the entrainment characteristics distinguished for near-field and self-similar regions. On the other hand, entrainment features of sprays are not as straightforward. The reason is that many unknown parameters and complicated phenomena affect the entrainment of sprays (Post et al., 2000). Influence of different parameters on the spray entrainment constant was studied by Post et al. (2000). Andriani et al. (1996) observed similarities in the entrainment characteristics of the gaseous jets and sprays in the transient period. On the other hand, they related the differences in the entrainment of the sprays and gaseous jets in the quasi-steady phase to their momentum transfer mechanisms. Sepret et al. (2010) divided the velocity field of the ambient gas into three regions, as shown in Fig. 4.1a. The first region close to the nozzle exit is called the quasi-steady zone. In the second region, ambient gas

is recirculated by the head vortex, and in the third zone the air is pushed out by the spray front. In Fig. 4.1a, gas normal velocity is shown for the mentioned zones. By temporal analysis of the gas velocity field, Sepret et al. (2010) showed that the near-exit entrainment region evolves with time. In Fig. 4.1b, variation of the velocity components normal to the spray axis with axial distance is shown.

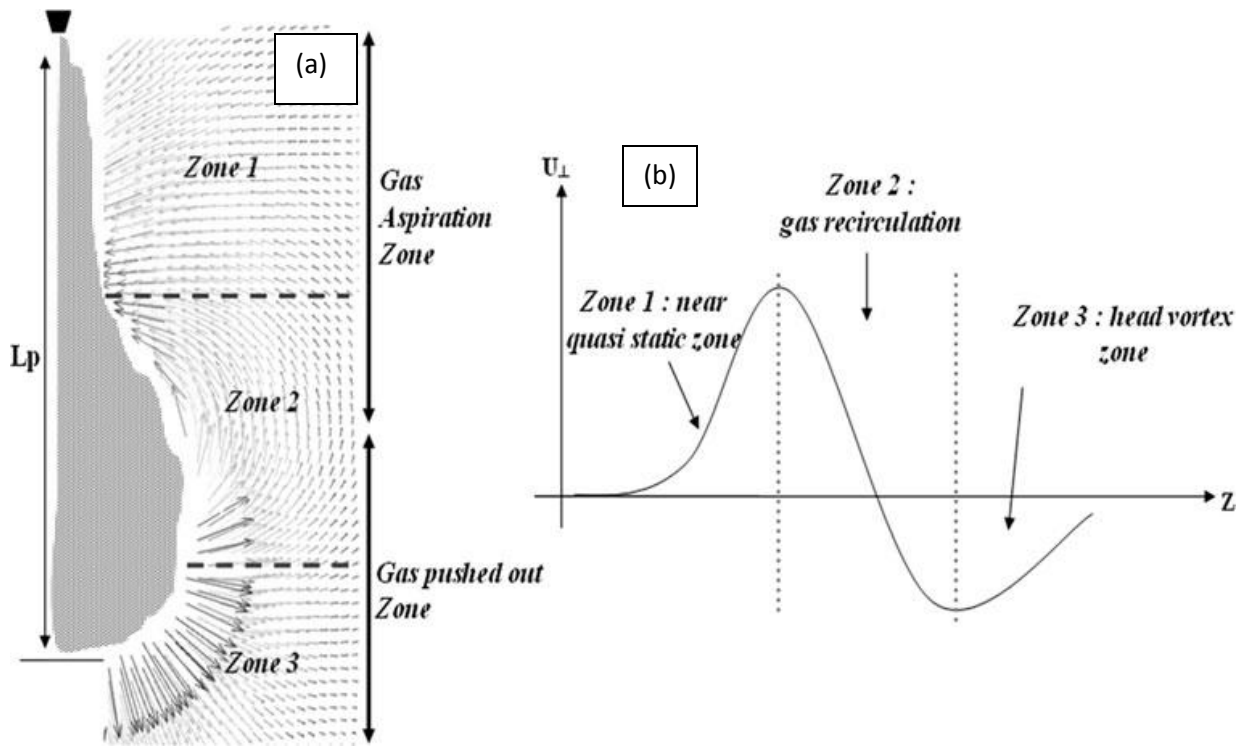


Figure 4.1: a) Mean gas velocity field; b) schematic evolution of the normal component of gas velocity (U_{\perp}), (Sepret et al., 2010)

Entrainment of the ambient air into the fuel spray can be related to different parameters such as spray cone angle expansion (Siebers, 1999) or fuel equivalence ratio distribution (Naber and Siebers, 1996).

In this Chapter, further study is performed on the cases studied in previous chapters, focusing on the air motion in diesel sprays. Air motion induced by the liquid movement

and droplet dispersion can be related to the air entrainment level. First, air entrainment into single diesel sprays are studied by incorporating CFD results into empirical equations. Then, the effect of different parameters on the entrainment behaviour resulting from empirical formulation is related to the identified vortex structure of the gaseous field. Deduced facts from the vortex structure assessment and its relation to air entrainment are used to analyze the air motion in merging sprays.

4.2 Results and Discussion

4.2.1 Empirical Assessment of the Entrainment in Single Sprays

By assuming that the spray and gaseous turbulent jets behave similarly, ambient air entrainment into the spray can be reasonably estimated with the same theory. The following formula approximates the equivalence ratio as the total amount of air entrained up to any axial location relative to the total amount of fuel injected (Naber and Siebers 1996):

$$\bar{\phi}(z) = \frac{2 (A/F)_{st}}{\sqrt{1 + 16 \left(\frac{z}{z^+}\right)^2 - 1}} \quad (20)$$

Where, $(A/F)_{st}$ is the stoichiometric air/fuel ratio. At each axial location of z , $\bar{\phi}(z)$ is the average value of the equivalence ratio in that cross-section, where z^+ is the characteristic length scale for the fuel jet, given by

$$z^+ = \sqrt{\frac{\rho_f}{\rho_a}} \frac{\sqrt{C_a} d_0}{a \tan(\theta/2)} \quad (21)$$

where a is a constant equal to 0.75 and C_a is orifice area contraction, taken to be 0.95. According to gaseous jet theory, Wang et al. (2010) used a Gaussian profile to achieve a radial distribution of the equivalence ratio:

$$\phi(z, r) = \phi_{axis}(z) \exp(-\alpha (r/R)^2) \quad (22)$$

The constant α is a shape factor for the Gaussian profile (Desantes et al. 2007) and $R = Z \tan(\theta/2)$. By assuming $\phi(z, R) = 0.1\phi_{axis}(z)$ the value for α is calculated as 2.3. The axial equivalence ratio is obtained as:

$$\phi_{axis}(z) = 2.55 \bar{\phi}(z) \quad (23)$$

Using analytical equations to calculate the spray tip penetration and cone angle, Wang et al. (2010) calculated axial (Fig 4.2) and radial (Fig 4.3) equivalence ratio distributions. These results are compared to our cases, which are combination of CFD and empirical formulations.

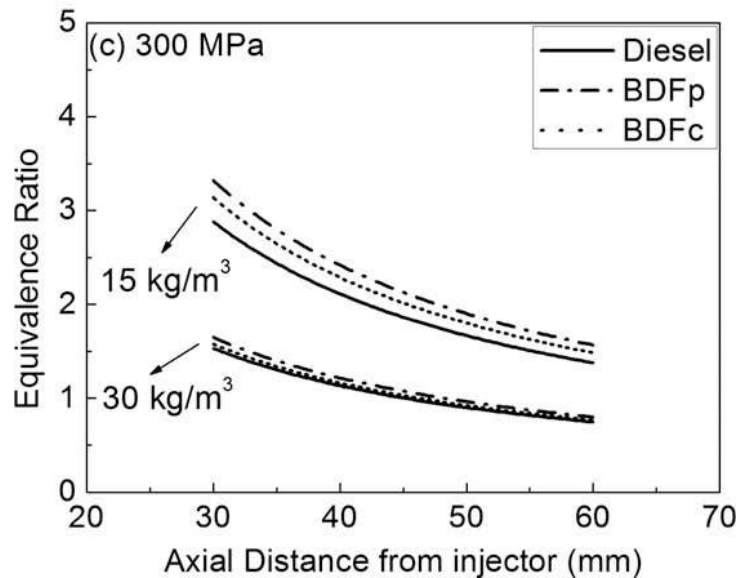


Figure 4.2: Empirical axial variation of equivalence ratio (Wang et al., 2010)

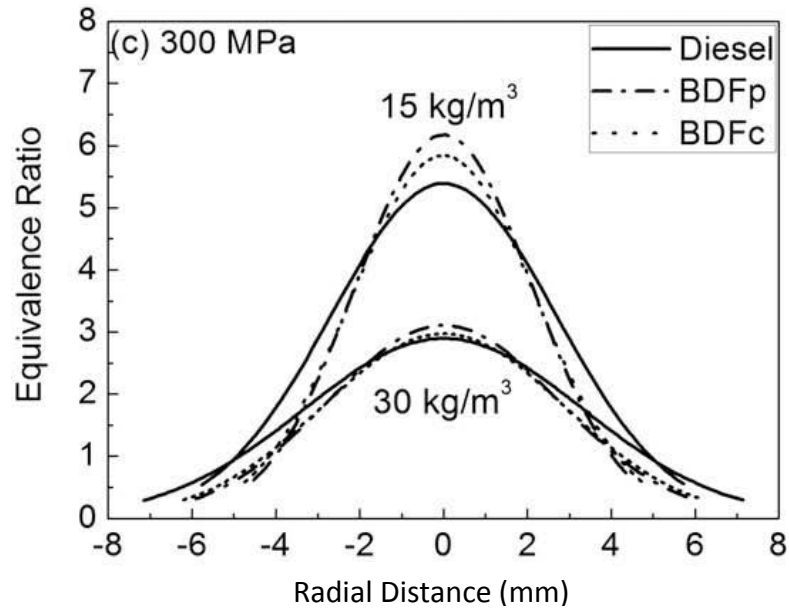


Figure 4.3: Empirical radial distribution of equivalence ratio (Wang et al., 2010)

In order to study the entrainment characteristics of single diesel sprays, CFD results acquired for the spray tip penetration and the spray cone angle have been incorporated in the above mentioned formulations. It should be mentioned that calculation of spray tip penetration and the cone angle have been validated in Chapter 2. For all the cases of the single diesel sprays the cone angle was calculated at $Z = 40$ mm of penetration. In Fig 4.4, axial variation of the equivalence ratio is shown for different injection pressures and ambient pressures. Up to 10 mm downstream of the nozzle there is a sharp drop in the equivalence ratio, while further downstream it approaches an asymptotic behavior. The initial drop in the near-field is as a result of rapid break-up of the spray, radial dispersion of the droplets, leading to the entrainment of the initially quiescent gas into the spray. The more air mixed with the fuel, the lower the equivalence ratio. Therefore, while travelling downstream a leaner mixture is observed. At higher injection pressures, higher relative velocity between the liquid and gas results in higher mixing rate and consequently a lower

equivalence ratio. Moreover, increasing the ambient density leads to a lower penetration of the spray and a larger cone angle. This larger expansion results in an improved entrainment. Comparing the current cases with the results discussed in Chapter 2, it can be seen that higher entrainment is usually associated with higher cone angles, especially in high ambient densities. These results are qualitatively in agreement by the purely empirical results of Wang et al. (2010) shown in Figures 4.2 and 4.3.

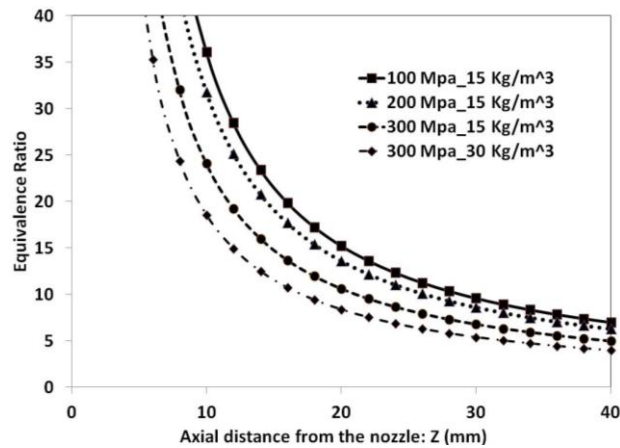


Figure 4.4: Axial variation of equivalence ratio

In Fig. 4.5 the effect of injection pressure on radial distribution of the equivalence ratio at an axial location of $Z = 20$ mm is shown. As can be seen, increasing the injection pressure results in a lower equivalence ratio which is a sign of higher entrainment. It is also observed that in any location, the equivalence ratio radial profile is more expanded for higher injection pressures. The higher expansion of the profile is a measure of more expansion in the spray as well as higher entrainment.

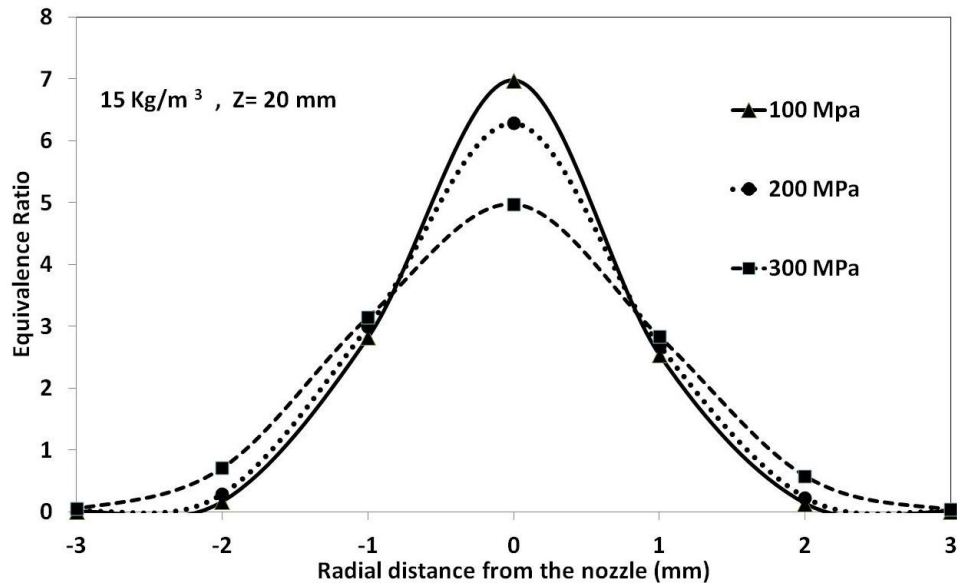
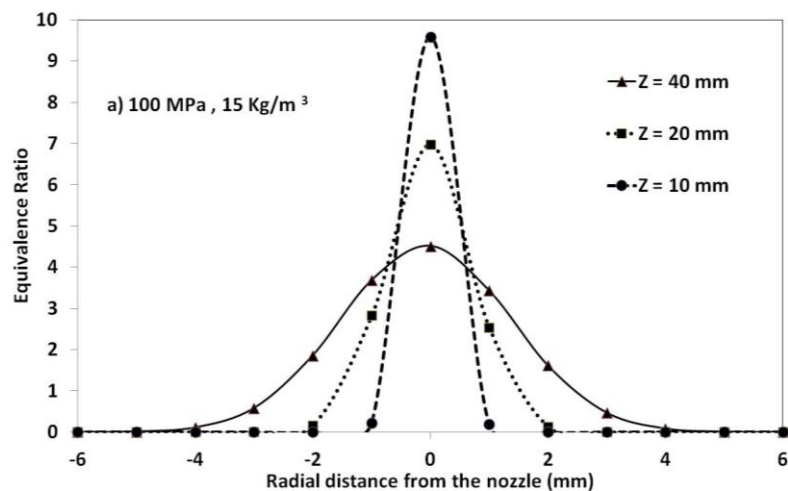


Figure 4.5: Effect of injection pressure on radial distribution of equivalence ratio at an axial location of $Z = 20$ mm

In Fig 4.6 the equivalence ratio radial profiles are compared at different axial locations for different injection pressures. For all the injection pressures it turns out that moving downstream, the equivalence ratio value drops. In addition, the radial equivalence ratio profiles expand in the spanwise direction. Magnitude reduction and profile expansion are both indications of air entrainment into the spray.



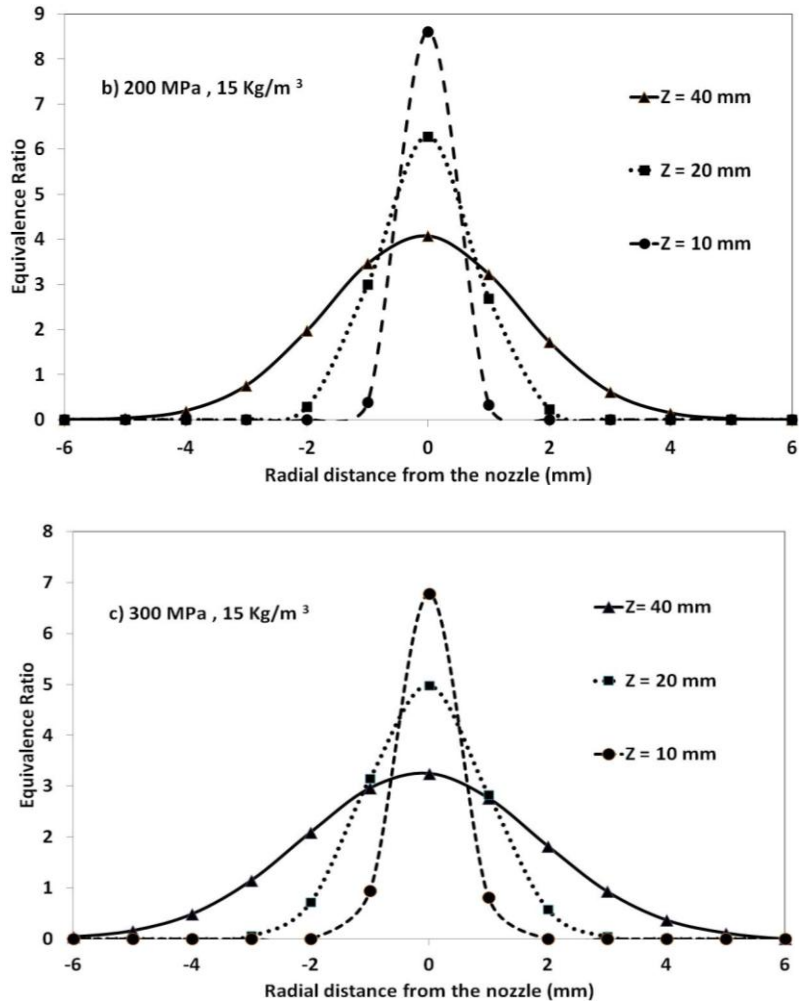


Figure 4.6: Variation of equivalence ratio radial distribution with axial location at different injection pressures: a) 100 MPa, b) 200 MPa, c) 300 MPa

The influence of ambient density on equivalence ratio radial distribution at an axial location of $Z = 40$ mm is shown in Fig. 4.7. In the case of higher ambient density the ambient gas decelerates the spray more strongly, resulting in a rapid expansion. As mentioned previously in Chapter 2, increasing ambient density leads to larger spray cone angles. Expansion of the spray is caused by the air entrainment. This fact is confirmed by focusing on the equivalence ratio profiles in Fig 4.7. In higher ambient density the profile

is expanded in the spanwise direction, while it gives lower values in the low ambient density case.

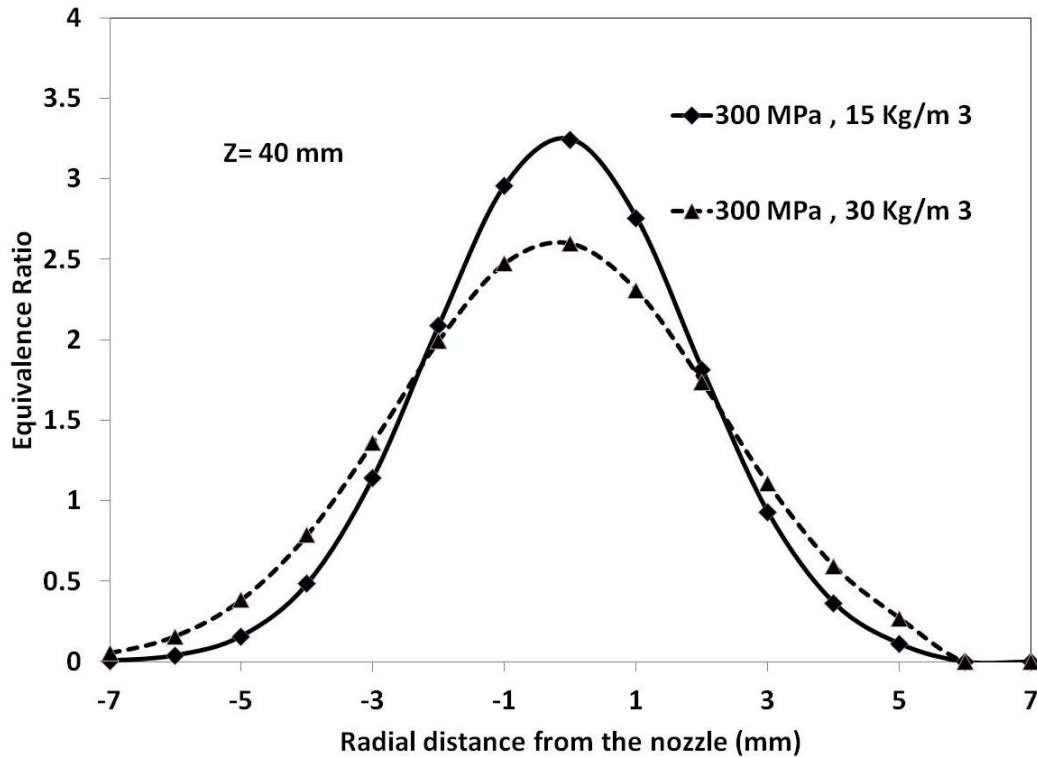


Figure 4.7: Effect of ambient density on equivalence ratio radial distribution at an axial location of $Z = 40$ mm

4.2.2 Air Motion Structure Induced by Spray Dispersion

In order to connect air motion structure to the entrainment behaviour of the spray, further analysis on the continuous phase pattern is required. To this end, vortex structures formed inside the spray which are attributed to the air motion are identified using velocity swirling strength. Swirling strength evaluates the local swirling motion of the flow field. Swirling strength is determined by analyzing the eigenvalues of the local velocity gradient tensor. Local swirling strength is identified as the imaginary part of the complex

eigenvalues of velocity gradient tensor (Zhou et al. 1999). The mathematical formulation of the swirling strength is presented in Appendix II.

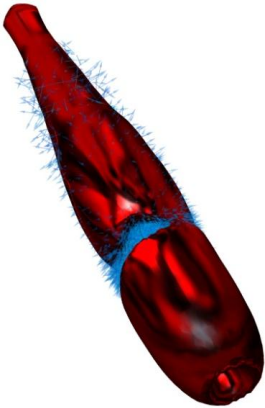
In this section vortex structures for single diesel sprays are identified first. The vortex patterns are connected to the entrainment analysis using the equivalence ratio. Then, vortex structures of the merging sprays are identified. According to the conclusions inferred from single spray vortex structure analysis, entrainment characteristics of the merging sprays are discussed.

Spray particle cloud superimposed by swirling strength iso-volumes of the gas are shown in Fig 4.8. Values of the swirling strength (λ) are normalized by the corresponding maximum (λ_{max}) value in each case. Three iso-values of $\frac{\lambda}{\lambda_{max}} = 0.15, 0.25, 0.5$ are obtained for three injection pressures of 100 MPa, 200 MPa, and 300 MPa and ambient density of $15 \frac{\text{Kg}}{\text{m}^3}$. Since the ambient air is initially quiescent, the gas motion is essentially induced by the liquid motion. The momentum transfer from the dispersed liquid to the gas phase generates a pattern similar to a gas jet inside the spray. Interestingly, for all the cases of the spray-induced gas jet, a region similar to quasi-steady and a pinched-off leading head vortex is observed. In the quasi-steady region, air is dragged into the spray, while in the tip of the spray the leading head vortex pushes the gas away. For larger values of $\frac{\lambda}{\lambda_{max}}$ smaller structures are identified. The larger swirl motion is generated in small structures to conserve their angular momentum. As can be seen, at higher injection pressures smaller structures are observed. Compared to Fig. 4.9 it can be seen that in the higher injection pressures higher turbulence intensity is induced in the gaseous phase by the liquid. The shear at the interface of gas and liquid generates instability. The higher

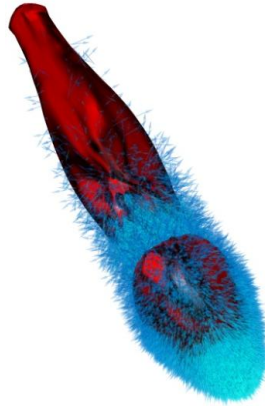
the instabilities the higher the turbulence intensity. These smaller structures are formed when in the higher injection pressures, higher shear and larger turbulence intensities are induced in the gas phase by fast moving liquid droplets. The highly disturbed gas in the case of high injection pressures mixes more quickly with the liquid phase. This confirms the entrainment analysis performed using the equivalence ratio. In other words, more entrainment in higher injection pressures observed in equivalence ratio profiles is associated with the formation of highly disturbed small structures.

The velocity vector field of the spray-induced air jet is shown in Fig 4.10. Comparing to Fig. 4.1a (Sepret et al., 2010), three different zones of the air motion are identifiable. In Zone 1, the quasi-steady zone is observed where the air velocity vectors are found to move inward into the spray as a result of the entrainment. This zone is called the gas aspiration zone. In Zone 2, which is called gas recirculation zone, ambient gas is recirculated in the wake of the leading head vortex. Zone 3 is called the gas pushed out zone, in which the air velocity vectors are pushed outward by the leading head vortex.

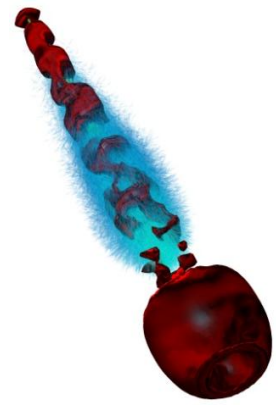
a) $100 \text{ MPa}, \frac{\lambda}{\lambda_{max}} = 0.15$



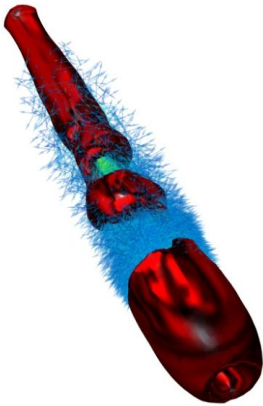
b) $200 \text{ MPa}, \frac{\lambda}{\lambda_{max}} = 0.15$



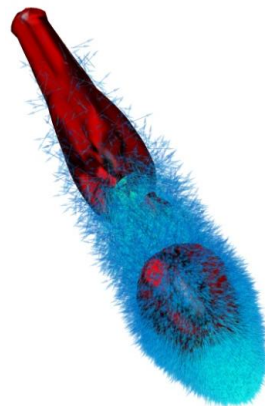
c) $300 \text{ MPa}, \frac{\lambda}{\lambda_{max}} = 0.15$



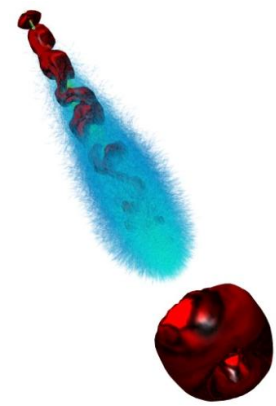
d) $100 \text{ MPa}, \frac{\lambda}{\lambda_{max}} = 0.25$



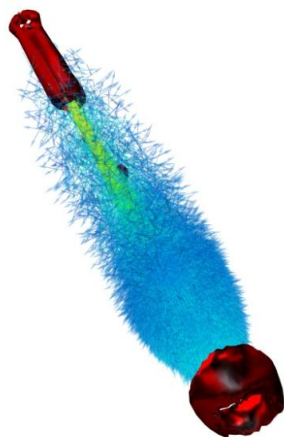
e) $200 \text{ MPa}, \frac{\lambda}{\lambda_{max}} = 0.25$



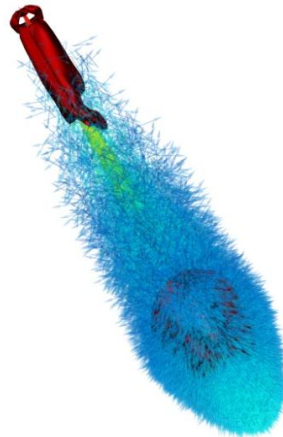
f) $300 \text{ MPa}, \frac{\lambda}{\lambda_{max}} = 0.25$



g) $100 \text{ MPa}, \frac{\lambda}{\lambda_{max}} = 0.5$



h) $200 \text{ MPa}, \frac{\lambda}{\lambda_{max}} = 0.5$



i) $300 \text{ MPa}, \frac{\lambda}{\lambda_{max}} = 0.5$

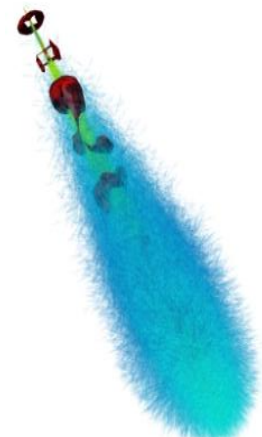


Figure 4.8: Single spray droplet cloud superimposed with swirling strength iso-volumes of the gas at $Z = 40 \text{ mm}$.

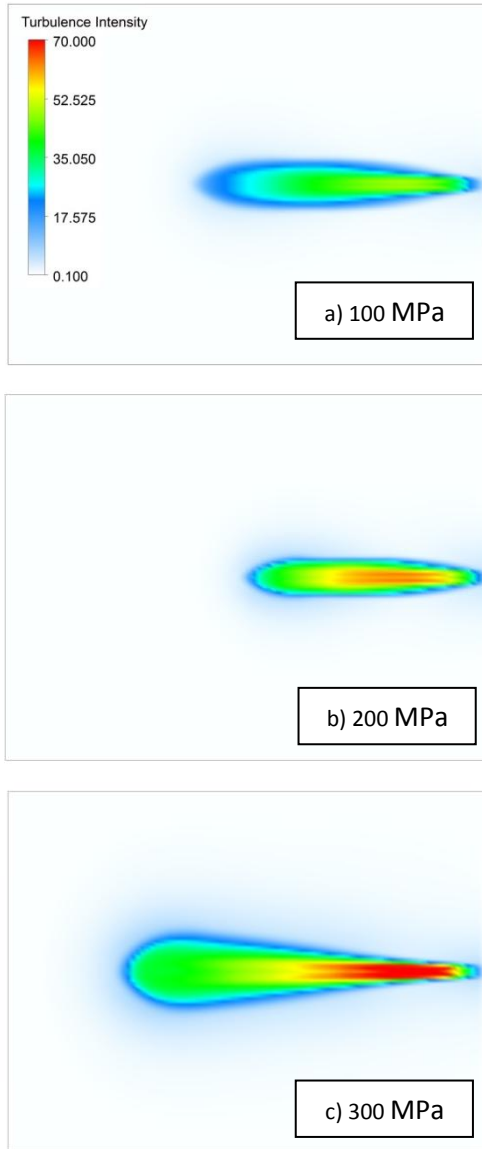


Figure 4.9: Turbulence intensity contour induced in the gas field in $X = 0$ plane at $Z = 40$ mm for different injection pressures

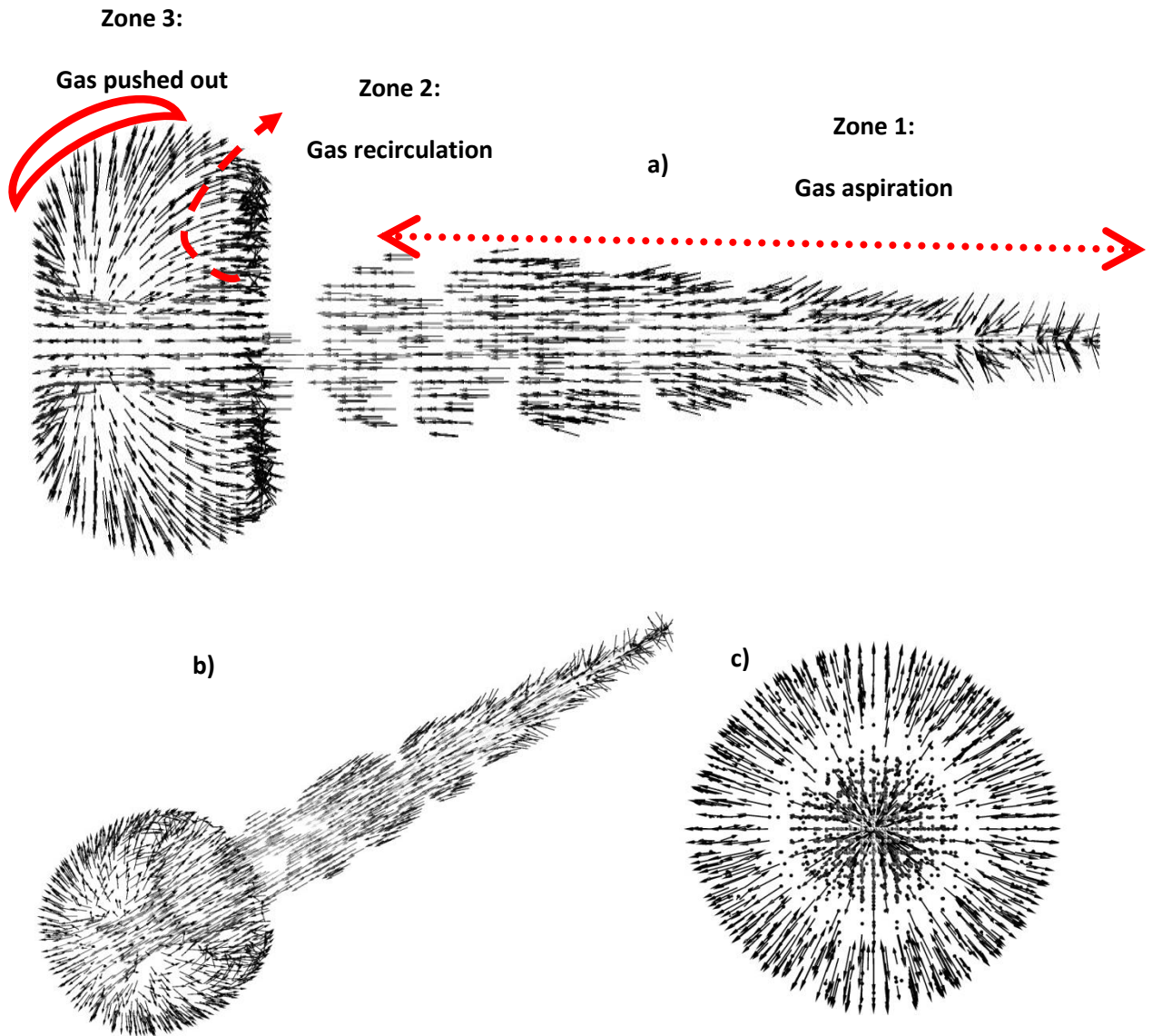


Figure 4.10: Velocity vector field of the air jet induced inside the spray at $Z = 40$ mm

In Fig 4.11, vortex cores of the gas phase, induced by the merging sprays are identified using swirling strength method. Injection pressure of each spray is 300 MPa and ambient air density is 15 Kg/m^3 . Iso-volumes of swirling strength ($\frac{\lambda}{\lambda_{max}} = 0.1$) are compared for different set-ups. Volumes of the identified structures are calculated and compared to gain knowledge about the entrainment behaviour. In the case of larger distance between the injection points larger structures are identified. In Chapter 3, larger distance resulted in

smaller cone angles of the merged spray. Both the large structures and the small cone angles are indications of lower entrainment into spray. At the larger distance sprays are more decelerated before reaching to the merging point. Lower momentum level of the liquid induces less disturbance in the gas phase and poor entrainment. In the case of $d = 10$ mm distance and incidence angle of $\varphi = 90^\circ$, the spray cone angle is maximum in both XZ and YZ planes. In addition, calculated volume of the vortex structures has the minimum value. Larger cone angles and smaller structures suggest higher entrainment inside the sprays. In the case of $d = 10$ mm distance and incidence angle of $\varphi = 90^\circ$, sprays merge in a shorter distance with larger momentum. In addition, merging with a higher relative velocity generates more disturbance and increases the level of turbulence intensity in the gaseous phase. More disturbance induced in the gas phase results in high swirl zones with smaller structures.

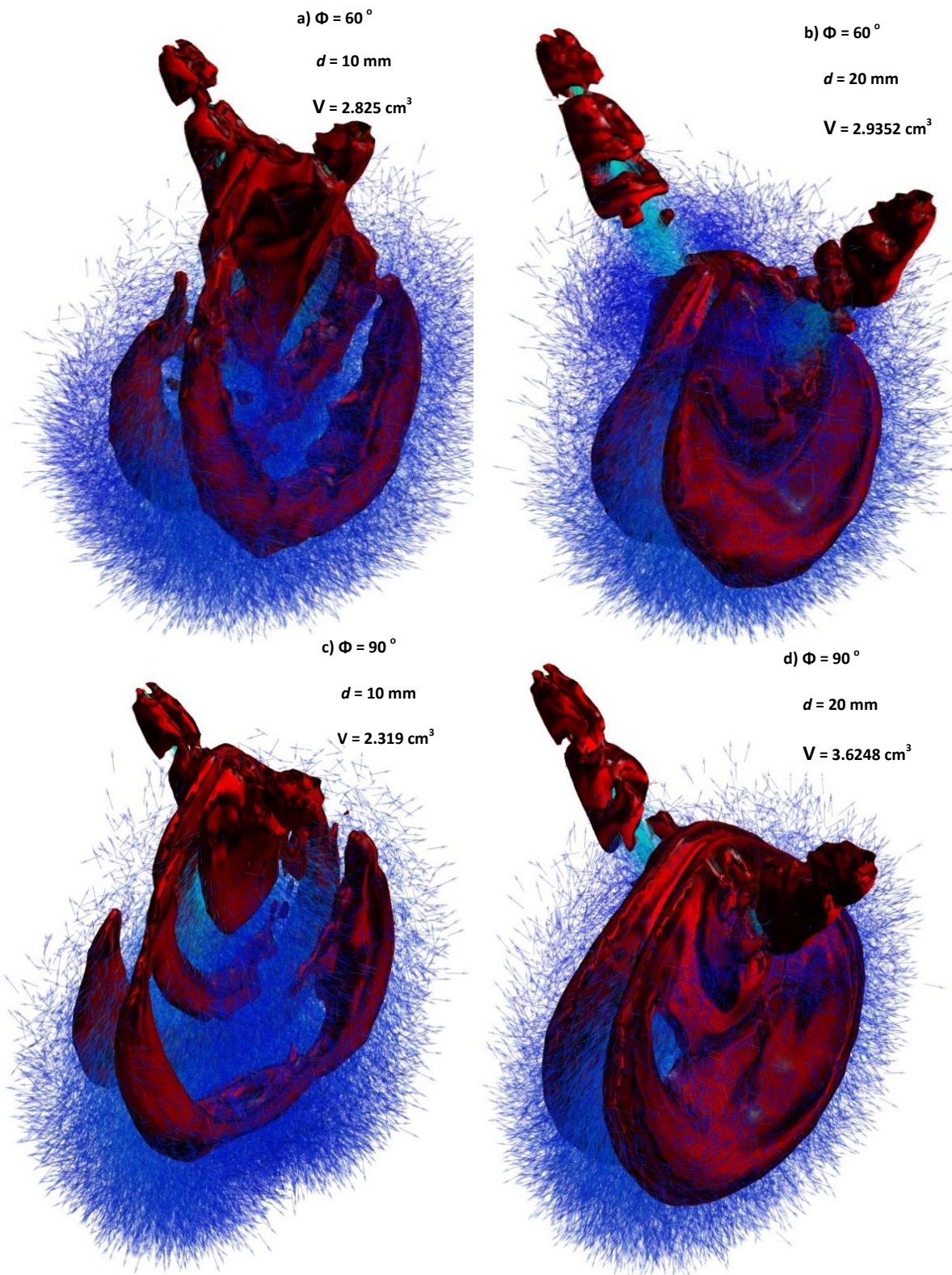


Figure 4.11: Merging spray droplet cloud superimposed on the iso-volume of swirling

strength $\left(\frac{\lambda}{\lambda_{\max}} = 0.1\right)$ at $t = 1 \text{ ms}$

4.3 Conclusions

In this chapter, further analysis was performed on the simulation cases of the previous chapters in terms of the air motion induced by the liquid dispersion. First, entrainment qualities of single diesel sprays were evaluated using a combination of the CFD and empirical formulations. Comparing the different equivalence ratio profiles in the axial and radial directions revealed that air entrainment is enhanced by increasing the injection pressure and ambient density. Then, it was shown that in higher injection pressures which contribute to more air motion, smaller vortex structures are formed. Larger swirling motion of the vortices was connected to the quality of the air entrainment. In addition, the vector field of the air jet induced inside the spray was analyzed and distinguishable zones of the gas motion were discussed. Finally, the idea of vortex structures was applied to the merging sprays to assess their entrainment qualities. Studying effects of injection location distance and incidence angle suggested that smaller highly rotating structures were formed at the lower distance and higher incidence angle. This was attributed to the higher entrainment and enhanced mixing.

CHAPTER 5

Conclusions and Recommendations

5.1 Conclusions

In this work, computational fluid dynamics (CFD) simulations were carried out to study the characteristics of diesel and biodiesel fuels. An Eulerian-Lagrangian approach was implemented to tackle the multiphase nature of the problem.

Chapter 1 introduces the processes that occur in full cone sprays, and a brief summary of the solution methods has been provided. In Chapter 2, results of the simulation of diesel and biodiesel sprays injected into an initially quiescent constant volume chamber are presented. The effect of various parameters such as injection pressure, ambient density, mesh structure, and break-up models on the spray behaviour have been investigated. The following conclusions are drawn from Chapter 2:

- In higher ambient densities, fuel sprays are strongly decelerated and yield a lower penetration.
- The Lagrangian description of the discrete phase shows a sensitivity to mesh structure, in spite of the independence of the results from the cell number.
- Spray penetration is almost independent of the break-up models used for this study in the linear phase of the penetration. On the other hand, further downstream in the asymptotic phase of the penetration, more sensitivity to the break-up model was observed. The reason for this behaviour is because in the near-field the

penetration is mostly affected by the momentum of the large droplets, while further downstream the break-up process has a greater influence.

- Biodiesel fuel sprays travel further into the chamber compared to the diesel fuel. This is due to their higher surface tension and viscosity which postpone the break-up process.
- Spray cone angle is found to be less influenced by the injection pressure, while it is highly dependent on the ambient density.
- Numerical simulations are able to reproduce the spray shape observed in experiments.
- Higher injection pressures result in a rapid drop in Sauter mean diameter (SMD) during the injection time, indicating a more successful break-up. In higher ambient density for any of the injection pressures, the rate of the SMD drop is slower due to the lower relative velocity of the gas and liquid.
- Rate of the SMD drop is smaller for biodiesel fuels due to their high surface tension. This necessitates the application of ultra-high injection pressures for biodiesel fuels.
- Droplet radial, axial, and temporal size distributions have been extensively discussed in Chapter 2 and connected to relevant processes of a fuel cone spray.

In Chapter 3, two diesel sprays injected from separated locations and merging in the downstream were simulated. The effects of nozzle location distance and incidence angle on the merged spray parameters can be summarized as follows:

- An interesting feature observed in the merging sprays is that the merged spray expands more in shorter penetration compared to single sprays. This results in enhanced entrainment.
- Contrary to single sprays which expand radially and axisymmetric, twin sprays expand differently in different planes.
- Increasing the nozzle separation distance (d) and decreasing the spray incidence angle (Φ) reduces the merged spray cone angles.
- Over-prediction of the coalescence by the O'Rourke model is caused by disregard for the collision break-up of the droplets. This was observed by the higher prediction of SMD compared to single sprays.
- Increasing the injection point distance (d) results in an increase in SMD, while increasing the incidence angle (Φ) leads to a reduction.

In chapter 4, air motion and entrainment characteristics of the single and merging sprays have been discussed:

- The axial equivalence ratio reduces while moving downstream as a result of the entrainment.
- Increasing injection pressure and ambient densities enhances the entrainment.
- Gaussian radial profiles of the equivalence ratio shows spanwise expansion and lower peak values in the high entrainment cases.
- In higher injection pressure single sprays which had improved entrainment, smaller vortex structures have been identified.

- Vector field analysis of the gas motion induced by the liquid dispersion illustrates distinguishable zones of gas aspiration, gas recirculation, and gas pushed out.
- Vortex cores were identified for different merging spray set-ups. Calculating the volume of the vortex core regions suggests that in the high entrainment cases the structures become smaller. For instance, smallest structure size was formed in the case with larger cone angle, due to the higher entrainment.

5.2 Contributions

Numerical simulation of the ultra-high injection pressure sprays of diesel and biodiesel fuels has revealed the necessity of using injection pressures up to 300 MPa to achieve improved atomization. Specially, ultra-high injection pressures were found to be more necessary for the biodiesel fuels to enhance their break-up. In addition, characteristics of the merging sprays such as lower penetration, more expansion, and enhanced entrainment can suggest a practical set-up for avoiding wall impingement in direct injection diesel engines. In previous studies in the literature, air motion outside the spray was connected to the entrainment characteristics of the sprays. In contrast, the focus of this study was to analyze gas motion inside the spray, where most of the mixing occurs due to the air motion. To this end, identification of the vortex structures in single and twin jets was used to disclose further knowledge about the gas motion induced by the liquid dispersion.

5.3 Recommendations

In order to acquire more information about the influence of the injection and spray parameters on the mixture formation in internal combustion engines, the following recommendations are suggested:

- Application of the different scenarios studied in this work to a real engine environment to bring out more realistic interaction of the spray with the ambient flow field. It is well-known that swirl and tumble flows in a high temperature environment can significantly influence spray processes.
- Extension of the simulations to the combustion phase to provide valuable information about the effect of the various parameters on the combustion and pollutant formation of IC engines.
- Connecting the gas vortex structure size to the level of entrainment yields some qualitative clues to the level of entrainment. However, it would be valuable to find a method to accurately quantify air motion through the structures.

REFERENCES

- Andriani R., Coghe A. and Cossali G. Near-Field Entrainment in Unsteady Gas Jets and Diesel Sprays: A Comparative Study, Twenty-Sixth Symposium (International) on Combustion, The Combustion Institute, Pittsburgh, PA, pp. 2549–2556, 1996
- Arai M. and Saito M. Atomization Characteristics of Jet-to-jet and Spray-to-spray Impingement Systems, *Atomization and Sprays*, Vol. 9 pp. 399-417, 1999
- Arcoumanis C., Gavaises M. and French B. Effect of Fuel Injection Process on the Structure of Diesel Sprays, SAE paper 970799, 1997
- Ashgriz N. Numerical Techniques for Simulating the Atomization Process, *Handbook of Atomization and Sprays*, Springer Verlag, Berlin, 2011
- Ashgriz N. and Poo J.Y. Coalescence and Separation in Binary Collisions of Liquid Drops, *J. Fluid Mech.*, Vol. 221, pp. 183–204, 1990
- Baumgarten C. *Mixture Formation in Internal Combustion Engines*, Springer-Verlag, Berlin, Heidelberg, ISBN-3 978-3-540-30835-5, 2006
- Beale J.C. and Reitz R.D. Modeling Spray Atomization with the Kelvin-Helmholtz/Rayleigh-Taylor Hybrid Model, *Atomization and Sprays*, Vol. 9, pp. 623-650, 1999
- Bianchi G.M., Pelloni P., Corcione F.E., Allocca L. and Luppino F. Modeling Atomization of High-Pressure Diesel Sprays, *Journal of Engineering for Gas Turbines and Power*, Vol. 123, pp. 419-427, 2001
- Demoulin F. X. and Borghi R. Modeling of Turbulent Spray Combustion with Application to Diesel Like Experiment, *Combustion and Flame*, Vol. 129(3), pp. 281-293, 2002

- Dhuchakallaya I. Watkins A. P., Numerical Modelling of Diesel Spray Auto-ignition and Combustion, *International Journal of Engine Research*, Vol. 12(2) pp. 169-180, 2011
- Diviš M. and Macek J. Fuel Injection Process Computations Using the Eulerian Multidimensional Model, SAE Technical Paper 2005-01-1243, SAE 2012 World Congress, Detroit, MI, 2005
- Djavareshkian M.H. and Ghasemi A. Investigation of Jet Break-Up Process in Diesel Engine Spray Modelling, *Journal of Applied Sciences*, Vol. 9 pp. 2078-2087, 2009
- Faeth GM. Evaporation and Combustion of Sprays, *Progress Energy Combust. Science*, Vol. 9, pp. 1–76, 1983
- Ejim C.M., Fleck B.A. and Amirfazli A. Analytical Study for Atomization of Biodiesels and Their Blends in a Typical Injector: Surface Tension and Viscosity Effects, *Fuel*, Vol. 86, pp. 1534–1544, 2007
- Fukuda K., Ghasemi A., Barron R.M. and Balachandar R. An Open Cycle Simulation of DI Diesel Engine Flow Field Effect on Spray Processes, SAE Technical Paper, 2012-01-0696, SAE 2012 World Congress, Detroit, MI, 2012
- Fu-shui L., Lei Z., Bai-gang S., Zhi-jie L. and Schock H.J. Validation and Modification of WAVE Spray Model for Diesel Combustion Simulation, *Fuel*, Vol. 87, pp. 3420–3427, 2008
- Ghasemi A., Fukuda K., Balachandar Ram. and Barron Ron. M. Numerical Investigation of Spray Characteristics of Diesel Alternative Fuels, SAE Technical Paper 2012-01-1265, SAE 2012 World Congress, Detroit, MI, 2012-a

Ghasemi A., Barron R.M. and Balachandar R. Spray-to-Spray Collision Breakup of Ultra High Injection Pressure Diesel Fuel, 20th Annual Conference of the CFD Society of Canada, Canmore, AB, May, 2012-b

Ghasemi A. and Djavareshkian M.H. Investigation of the Effects of Natural Gas Equivalence Ratio and Piston Bowl Flow Field on Combustion and Pollutant Formation of a DI Dual Fuel Engine, Journal of Applied Sciences, Vol. 10, pp. 1369-1379, 2010

Gosman A.D. and Ioannides E. Aspects of Computer Simulation of Liquid-Fueled Combustors, AIAA Paper No 81-0323, American Institute of Aeronautics and Astronautics, Aerospace Sciences Meeting, 19th, St. Louis, Mo., 1981

Huang Z., State Key Laboratory of Multiphase Flow in Power Engineering, Xi'an Jiaotong University, Xi'an 710049, Republic of China, Personal communication, E-mail address: zhhuang@mail.xjtu.edu.cn

Jaime A., Erazo Jr., Parthasarathy R. and Gollahalli S. Atomization and Combustion of Canola Methyl Ester Biofuel Spray, Fuel, Vol. 89 pp. 3735–3741, 2010

Kim H.J., Park S.H. and Lee C.S. A Study on the Macroscopic Spray Behavior and Atomization Characteristics of Biodiesel and Dimethyl Ether Sprays Under Increased Ambient Pressure, Fuel Processing Technology, Vol. 91, pp. 354–363, 2010

Ko G.H. and Ryou H.S. Droplet Collision Processes in an Inter-spray Impingement System, Aerosol Science, Vol. 36, pp. 1300–1321, 2005

- Lee S.H., Ko G.H. and Ryou H.S. A Numerical Study on the Spray-to-spray Impingement System, KSME International Journal, Vol. 16, 235–245, 2002
- Lee W. G. and Reitz R. D. A Numerical Investigation of Transient Flow and Cavitation Within Minisac and Valve-Covered Orifice Diesel Injector Nozzles, Journal of Engineering for Gas Turbines and Power, Vol. 132, pp. 052802-1, 2010
- Lin Y. S. and Lin H. P. Spray Characteristics of Emulsified Castor Biodiesel on Engine Emissions and Deposit Formation, Renewable Energy, Vol. 36, pp. 3507-3516, 2011
- Merker G. P., Schwarz C., Stiesch G. and Otto F. Simulating Combustion: Simulation of Combustion and Pollutant Formation for Engine Development, P: 343-347, Springer-Verlag Berlin Heidelberg, ISBN 10 3-540-25161-8, 2006
- Naber J.D and Siebers D.L. Effects of Gas Density and Vaporization on Penetration and Dispersion of Diesel Sprays, SAE Technical Paper 960034, SAE World Congress, Detroit, MI, 1996
- Ohnesorge W. Die Bildung von Tropfen an Düsen und die Auflösung flüssiger Strahlen. Zeitschrift für angewandte Mathematik und Mechanik, Bd.16, Heft 6, pp 355–358, 1931
- O'Rourke P.J. Collective Drop Effects on Vaporizing Liquid Sprays, PhD Dissertation, Department of Mechanical and Aerospace Engineering, Princeton University, 1981
- Park S. H., Kim H. J., Suh H. K. and Lee C. S. Experimental and Numerical Analysis of Spray-atomization Characteristics of Biodiesel Fuel in Various Fuel and Ambient

- Temperatures Conditions, International Journal of Heat and Fluid Flow, Vol. 30, pp. 960–970, 2010
- Park S. H., Kim H, J. and Lee C. S. Comparison of Experimental and Predicted Atomization Characteristics of High-pressure Diesel Spray Under Various Fuel and Ambient Temperature, Journal of Mechanical Science and Technology, Vol. 24 (7) pp. 1491-1499, 2010
- Post S., Iyer V. and Abraham J. A Study of Near-Field Entrainment in Gas Jets and Sprays Under Diesel Conditions, Journal of Fluids Engineering, Vol. 122, pp. 385-395, 2000
- Reitz, R.D. and Diwakar Structure of High-Pressure Fuel Sprays, SAE Paper, No.870598, pp1-18, SAE World Congress, Detroit, MI, 1987
- Roisman I.V., Araneo L. and Tropea C. Effect of Ambient Pressure on Penetration of a Diesel Spray, International Journal of Multiphase Flow, Vol. 33, pp. 904–920, 2007
- Sepret V., Bazile R., Marchal M. and Couteau G. Effect of Ambient Density and Orifice Diameter on Gas Entrainment by a Single-hole Diesel Spray, Experiments in Fluids, Vol. 49, pp. 1293–1305, 2010
- Siebers D. L. Scaling Liquid-phase Penetration in Diesel Sprays Based on Mixing-limited Vaporization, SAE Paper No. 1999-01-0528, SAE World Congress, Detroit, MI, 1999
- Som S., Aggarwal S. K., El-Hannouny E. M. and Longman D. E. Investigation of Nozzle Flow and Cavitation Characteristics in a Diesel Injector, Journal of Engineering for Gas Turbines and Power, Vol. 132, 042802, pp. 1-12, 2010

- Som S. and Aggarwal S.K. Effects of Primary Breakup Modeling on Spray and Combustion Characteristics, *Combustion and Flame*, Vol. 157, pp. 1179–1193, 2010
- Som S., Ramirez A. I. and Longman D. E. and Aggarwal S. K. Effect of Nozzle Orifice Geometry on Spray Combustion and Emission Characteristics under Diesel Engine Conditions, *Fuel*, Vol. 90, pp. 1267–1276, 2011
- Trinh H. P. and Chen C. P. Balasubramanyam M. S. Numerical Simulation of Liquid Jet Atomization Including Turbulence Effects, *Journal of Engineering for Gas Turbines and Power*, Vol. 129, pp. 920-928, 2007
- Tsuru D., Tajima H., Ishibashi R. and Kawauchi S. Droplet Collision Modelling Between Merging Immiscible Sprays in Direct Water Injection System, ILASS–Europe 2010, 23rd Annual Conference on Liquid Atomization and Spray Systems, Brno, Czech Republic, 2010
- Wang X., Huang Z., Kuti O. A., Zhang W. and Nishida K. Experimental and Analytical Study on Biodiesel and Diesel Spray Characteristics under Ultra-high Injection Pressure, *International Journal of Heat and Fluid Flow*, 31 659–666, 2010
- Wang Y., Lee W. G. and Reitz R. and Ramachandra Diwakar Numerical Simulation of Diesel Sprays Using an Eulerian-Lagrangian Spray and Atomization (ELSA) Model Coupled with Nozzle Flow, SAE 2011-01-0386, SAE World Congress, Detroit, MI, 2011
- Watkins A. P. Numerical Modelling of Diesel Spray Auto-ignition and Combustion, *International Journal of Engine Research*, Vol. 12 (2), pp. 169-180, 2011

Wierzba A Deformation and Breakup of Liquid Drops in a Gas Stream at Nearly Critical Weber Numbers, *Experiments in Fluids*, Vol 9, pp. 59–64, 1993

Zhang J. and Fang T. Spray Combustion of Biodiesel and Diesel in a Constant Volume Combustion Chamber, SAE 2011-01-1380, 2011

Zhou J., Adrian R. J., Balachandar S. and Kendall T. M. Mechanisms for Generating Coherent Packets of Hairpin Vortices, *J. Fluid Mech.* Vol. **387**, pp. 353–396, 1999

APPENDICES

Appendix I Eulerian-Lagrangian Multiphase Flow Equations

As it was mentioned in previous chapters continuous phase is simulated by solving Reynolds averaged Navier-Stokes (RANS) equations coupled by turbulence $k - \varepsilon$ model:

$$\frac{\partial \rho}{\partial t} + \frac{\partial}{\partial x_i} (\rho u_i) = 0 \quad (24)$$

$$\frac{\partial}{\partial t} (\rho u_i) + \frac{\partial}{\partial x_j} (\rho u_i u_j) = -\frac{\partial P}{\partial x_i} + \frac{\partial}{\partial x_j} \left[\mu \left(\frac{\partial u_i}{\partial x_j} + \frac{\partial u_j}{\partial x_i} - \frac{2}{3} \delta_{ij} \frac{\partial u_l}{\partial x_l} \right) \right] + \frac{\partial}{\partial x_j} (-\rho \overline{u'_i u'_j}) \quad (25)$$

where $-\rho \overline{u'_i u'_j}$ is called Reynolds stresses. Using Boussinesq hypothesis the Reynolds stresses are related to mean velocity gradients:

$$-\rho \overline{u'_i u'_j} = \mu_t \left(\frac{\partial u_i}{\partial x_j} + \frac{\partial u_j}{\partial x_i} \right) - \frac{2}{3} (\rho k + \mu_t \frac{\partial u_k}{\partial x_k}) \delta_{ij} \quad (26)$$

where μ_t is the turbulent viscosity which is related to turbulence kinetic energy (k) and turbulence dissipation rate (ε):

$$\mu_t = \rho C_\mu \frac{k^2}{\varepsilon} \quad (27)$$

Turbulence kinetic energy (k) and turbulence dissipation rate (ε) are determined solving following transport equations:

$$\frac{\partial}{\partial t} (\rho k) + \frac{\partial}{\partial x_i} (\rho k u_i) = \frac{\partial}{\partial x_j} \left[\left(\mu + \frac{\mu_t}{\sigma_k} \right) \frac{\partial k}{\partial x_j} \right] + G_k + G_b - \rho \varepsilon + Y_M + S_k \quad (28)$$

$$\frac{\partial}{\partial t} (\rho \varepsilon) + \frac{\partial}{\partial x_j} (\rho \varepsilon u_j) = \frac{\partial}{\partial x_j} \left[\left(\mu + \frac{\mu_t}{\sigma_\varepsilon} \right) \frac{\partial \varepsilon}{\partial x_j} \right] + C_{1\varepsilon} \frac{\varepsilon}{k} (G_k + C_{3\varepsilon} G_b) - C_{2\varepsilon} \rho \frac{\varepsilon^2}{k} + S_\varepsilon \quad (29)$$

On the other hand, discrete phase is treated using a Lagrangian approach. In this method the dispersed phase interacts with the continuous phase by the sub-models defined in the previous chapters. Trajectories of the individual particles are calculated by integrating the

following equation. This equation is resulted by the balance of particle inertia with the forces applied on the particle:

$$\frac{du_p}{dt} = F_D(U - U_p) + \frac{g_x(\rho_p - \rho)}{\rho_p} + F_x \quad (30)$$

where F_x is an additional acceleration term (force per unit mass of the particle), and $F_D(U - U_p)$ is the drag force per unit mass of the particle:

$$F_D = \frac{18\mu}{\rho_p d_p^2} \frac{C_D Re}{24} \quad (31)$$

where, u is the gas phase velocity, u_p is the particle velocity, μ is the molecular viscosity of the gas phase, ρ is the gas density, ρ_p is the particle density, d_p is the particle diameter, and Re is the relative Reynolds number, where Reynolds number is defined as:

$$Re = \frac{\rho d_p |u_p - u|}{\mu} \quad (32)$$

Appendix II Swirling Strength

Swirling strength is a measure of the swirling motion of the local structures around a center and is used to identify vortex regions in the flow field. The imaginary part of the eigenvalues of the instantaneous velocity gradient tensor (D) is called swirling strength (Zhou et al. 1999):

$$D = [d_{ij}] = \begin{bmatrix} d_{11} & d_{12} & d_{13} \\ d_{21} & d_{22} & d_{23} \\ d_{31} & d_{32} & d_{33} \end{bmatrix} = \begin{bmatrix} \frac{\partial u}{\partial x} & \frac{\partial u}{\partial y} & \frac{\partial u}{\partial z} \\ \frac{\partial v}{\partial x} & \frac{\partial v}{\partial y} & \frac{\partial v}{\partial z} \\ \frac{\partial w}{\partial x} & \frac{\partial w}{\partial y} & \frac{\partial w}{\partial z} \end{bmatrix} \quad (33)$$

Following equation yields the eigenvalues of the velocity gradient tensor:

$$\lambda^3 + P\lambda^2 + Q\lambda + R = 0 \quad (34)$$

where

$$P = -\text{tr}(D) = -\nabla \cdot \mathbf{u} = -(d_{11} + d_{22} + d_{33}) \quad (35)$$

$$Q = \frac{1}{2}[P^2 - \text{tr}(DD)] =$$

$$(d_{22}d_{33} - d_{23}d_{32}) + (d_{11}d_{22} - d_{12}d_{21}) + (d_{33}d_{11} - d_{11}d_{33}) \quad (36)$$

$$R = \frac{1}{3}[-P^3 + 3PQ - \text{tr}(DDD)] =$$

$$d_{11}(d_{23}d_{32} - d_{22}d_{33}) + d_{12}(d_{21}d_{33} - d_{31}d_{23}) + d_{13}(d_{31}d_{22} - d_{21}d_{32}) \quad (37)$$

Now let

$$q = Q - \frac{1}{3}P^2 \quad (38)$$

$$r = R - \frac{2}{27}P^3 - \frac{1}{3}PQ \quad (39)$$

For a positive discriminant the tensor has one real eigenvalue λ_r and a pair of conjugated complex eigenvalues $\lambda_{cr} + i\lambda_{ci}$. Then the tensor can be decomposed as:

$$[d_{ij}] = [v_r \ v_{cr} \ v_{ci}] \begin{bmatrix} \lambda_r & 0 & 0 \\ 0 & \lambda_{cr} & \lambda_{ci} \\ 0 & -\lambda_{ci} & \lambda_{cr} \end{bmatrix} [v_r \ v_{cr} \ v_{ci}]^{-1} \quad (40)$$

If

$$\zeta_2 = \sqrt{\sqrt{\Delta} - \frac{r}{2}} \quad (41)$$

and

$$\zeta_3 = \sqrt{\sqrt{\Delta} + \frac{r}{2}} \quad (42)$$

Then

$$\lambda_r = \widetilde{\lambda}_r - \frac{P}{3} = \zeta_2 - \zeta_3 - \frac{P}{3} \quad (43)$$

$$\lambda_{cr} = \widetilde{\lambda}_r - \frac{P}{3} = -\frac{\zeta_2 - \zeta_3}{2} - \frac{P}{3} \quad (44)$$

$$\lambda_{ci} = \frac{\zeta_2 + \zeta_3}{2} \sqrt{3} \quad (45)$$

λ_{ci} is called swirling strength which represents the strength of the local swirling motion.

The direction of the swirling vector is that of the real eigenvector v_r .

COPYRIGHT PERMISSION

From:	Terri Kelly <terri@sae.org>
Subject:	RE: COPYRIGHT 12PFL-0103/2012-01-1265
Date:	Mon, 21 May 2012 14:24:18 +0000
To:	Gina Brandon <gbrandon@sae.org>, "ghasemi@uwindsor.ca" <ghasemi@uwindsor.ca>, Darlene Fritz <dfritz@sae.org>

Dear Mr. Ghasemi,
Thank you for your correspondence requesting permission to include SAE paper 2012-01-1265 - which you co-authored - as part of your thesis for University of Windsor.

Permission is hereby granted, and subject to the following conditions:

- Permission is for this one-time use only. New requests are required for further use or distribution of the SAE material.
- The following credit statement must appear on the paper: "Reprinted with permission from SAE Paper No. 2012-01-1265 © 2012 SAE International. Further use or distribution is not permitted without permission from SAE."
- This permission does not cover any third party copyrighted work which may appear in the material requested.

Please note that SAE usually requires a six-month exclusive distribution period for our technical papers, which would not allow distribution of this paper until October 2012. However, we understand that you need this material for your thesis, and will allow you to include this paper in your thesis with distribution limited to this use only. Further use or distribution of this paper should not happen until after October 25, 2012.

Please feel free to contact me if you need further assistance.

Best regards,
Terri Kelly
Intellectual Property Rights Administrator

SAE International | 400 Commonwealth Drive | Warrendale, PA 15096-0001 | USA
Office: +01 724-772-4095 | Fax: +01 724-776-9765



VITA AUCTORIS

Personal Information

First Name: Abbas
Last Name: Ghasemi
Place of Birth: Behshahr, Iran
Year of Birth: 1980

Education

M.Sc. Mechanical Engineering, Energy Conversion,
(2008) University of Tabriz, Tabriz, Iran.

B.Sc. Mechanical Engineering, Fluid Mechanics, University of Tabriz. Tabriz,
(2005) Iran.